# Cosmogenic data about offset uplifted river terraces and erosion rates: implication regarding the central North Anatolian Fault and the Central Pontides

Aurélia Hubert-Ferrari, Laureen Drab, Jerome van Der Woerd, Lucilla Benedetti, Jean van Campenhout

# Cosmogenic data about uplifted river terraces and erosion rates: Implication regarding the central North Anatolian Fault and the Central Pontides

**Aurélia Hubert-Ferrari[1], Laureen Drab[2], Jérome Van Der Woerd[3], Lucilla Benedetti[4] and Jean Van Campenhout[1]**

[1] Department of Geography, Sart Tilman, Quartier Village 4, clos Mercator 3, B- 4000 Liège 1, Belgium.

[2] Beicip Franlab, 92502 Rueil-Malmaison, France.

[3] Active Tectonique IPGS-EOST, 5, rue René Descartes, 67084 Strasbourg, France.

[4] CEREGE UMR CNRS 6635, Université Aix-Marseille III, BP 80 Europole Méditerranéen de l'Arbois, 13545 Aix en Provence, France

Corresponding author: Aurelia and Hubert-Ferrari (aurelia.ferrari@uliege.be)

**Key Points:**

- 1 mm/yr uplift along the central transpressive segment of the North Anatolian Fault
- Maximum geological slip rate of 14 mm/yr for the central North Anatolian Fault over the last 85ka
- MIS 5a strath planation along the Kizilirmak River corresponds to a major Mediterranean river aggradation event and to high denudation rate in the Central Pointides mountains
- Variable displacement per event along the central segment of the North Anatolian Fault that last ruptured in 1943 and 1668.
- Holocene cosmogenic-based denudation rates in the Central Pontides are high and mostly controlled by tectonics
- Cumulated deformation in the Central Pontides is only partly controlled and induced by the North Anatolia Fault
- Frost-cracking in carbonate mountains is a dominant mechanism during Glacial Periods

## Abstract

River terraces are geomorphological markers recording deformation. Here, we use river terraces along the Kızılırmak River in Turkey to unravel the transpressive deformation along the convex arc formed by the central North Anatolian Fault (NAF), a continental transform fault. $^{10}$Be, $^{26}$Al, $^{36}$Cl cosmogenic exposure ages of T3 and T2 strath terraces constrained their formation at 85±15ka and 66±7.8ka, respectively, during climatic degradations and evidenced frost-cracking occurrence bringing younger carbonate cobbles on them. T1, a younger fill terrace was probably emplaced during the last glacial-interglacial transition. Terraces were deformed. The most recent one records the cumulated 14±2m deformation of the 1944 and 1668 earthquakes. T3 offset by 750 m constrains a geological slip rate of 8 to 14 mm/yr comparable to the 15 mm/yr geological rate of the Kızılırmak River over 2 Ma. T2 and T3 evidenced an uplift of 1 mm/yr. Compared to the 0.28 mm/yr obtained in the adjacent catchment, a larger portion of the shortening in the Central Pontides is accommodated close to the driving plate boundary, the NAF. We also evidenced high cosmogenic-based erosion rates in Pontides during the Holocene, and even higher rates during T3 planation. Erosion rates were combined with present-day relief to infer a first order minimal shortening of 12-16 km using simple mass balance principles. This long-term shortening is larger that the one induced by the Anatolian rotation suggesting a far field effect of the collision.


## 1 Introduction

For a transform plate boundary, the plate relative motion is defined by the rotation around a given eularian pole, and a pure transform fault follows a small circle around this pole. When the transform fault geometry differs from a small circle, it results into extensional or compressional deformation. Over the life span of the fault, large subsiding sedimentary basins and mountain ranges are thus formed. An example of the later is the convex bend of the North Anatolian Transform Fault (NAF) in its central part.

The NAF in the eastern Mediterranean area is a ~1500 km long right-lateral transform fault and its geometry is similar to a small circle around an Eulerian pole located near the Sinai [*Reilinger et al.,* 2006]. The NAF accommodates the extrusion of the Anatolian microplate westward toward the Aegean subduction zone (Figure 1). Here we focus on its central northward convex arc where the fault curvature is narrower than the ideal small circle for a smooth rotation of the Anatolian microplate (Figure 1). The fault geometry generates a large compressional fault-normal deformation accommodated in a ~200 km wide area called the Central Pontides (CP), which also defines the northern edge of the uplifted Central Anatolian Plateau (CAP). Compression in the CP is attested by a wide array of evidences. Geodetic observations show that the Anatolian motion with respect with Eurasia is not parallel to the NAF, implying a significant compressive deformation (Figure 1) [*Kreemer et al.,* 2003; *Reilinger et al.,* 2006; *Allmendinger et al.,* 2007; *Yavaşoğlu et al.,* 2011]. Active uplift in the CP is confirmed by regional morphometry and geomorphic observations by *Yıldırım et al.* [2011, 2013a]; they proposed a geodynamical model where the CP would be an active orogenic wedge extending from the CAP to the Black Sea coast. Deformation would result from a positive flower-structure geometry and be developed over a shallow detachment surface linked to the NAF at depth.

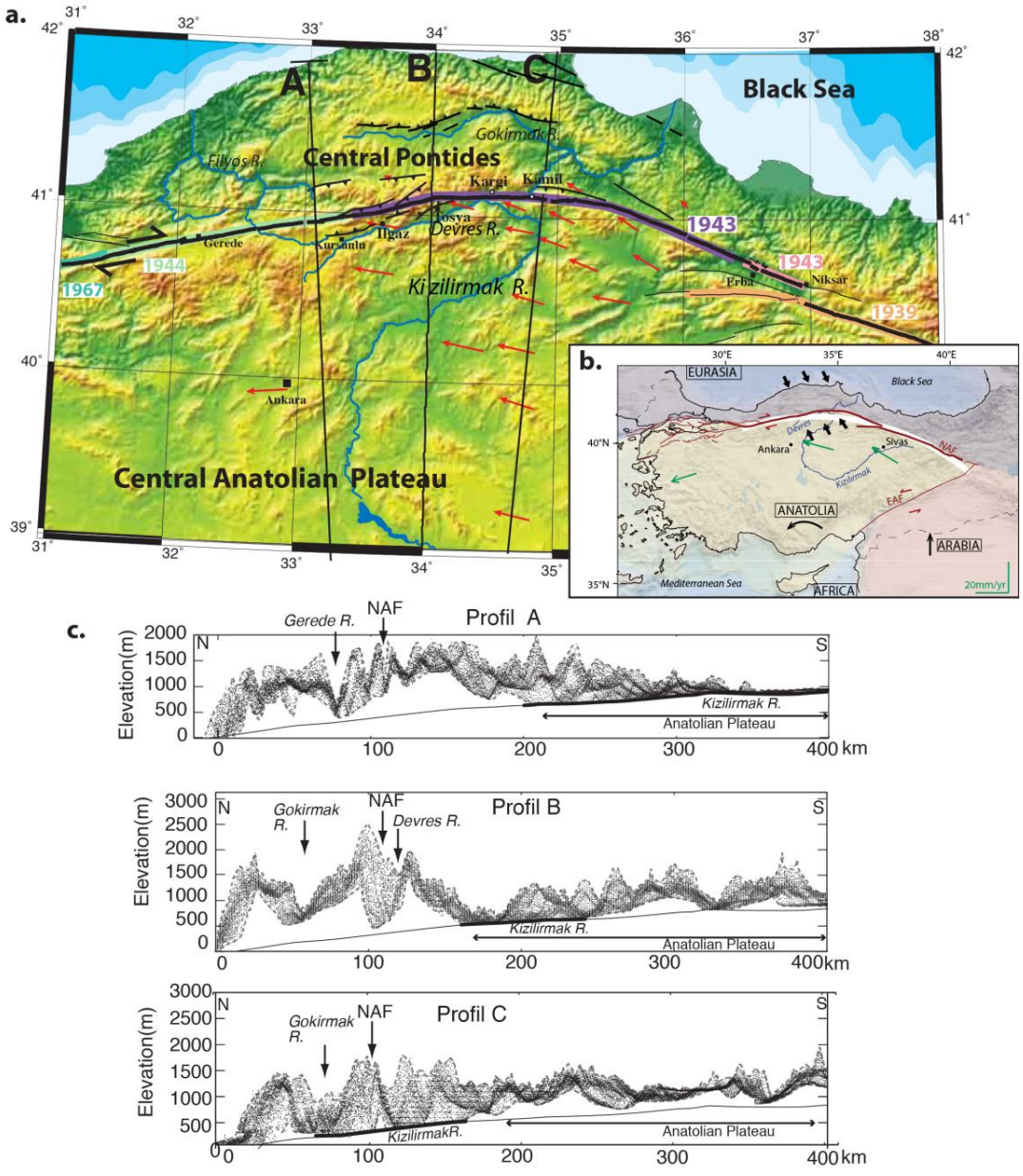


**Figure 1**. Geodynamic setting. **a**. The central NAF forming a broad convex arc, and secondary thrust faulting of the CP orogenic wedge; river network indicated in blue; location of the three A, B, C profiles displayed below in Figure 1c. **b**. Inset with the Anatolian plate bounded to the north by the NAF; thick white line indicates the geometry of the Eulerian small circle. **c**. Three swath profiles perpendicular to the NAF evidencing the relief of the CP resulting from shortening.

The relationship between the NAF strike-slip motion and shortening within the CP wedge still remains an open question. We focus here on a set of strath and fill terraces mostly in the Kargi Basin that are deformed by the NAF and on watersheds potentially affected by folding and thrusting along the NAF. Regarding the former, we used terrestrial cosmogenic exposure dating to constrain the terrace ages; for the later cosmogenic based erosion rates

constrain Holocene denudation rates in the CP. Geomorphological and cosmogenic data allow us to discuss the terrace formation, origin and incision, to infer a new geological slip rate along the central NAF, to evaluate the uplift gradient in the CP and to obtain a first-order evaluation of cumulated shortening in the CP to be compared with the one deduced from the NAF kinematics.

## 2 Tectonic Geomorphology of the NAF along its central part

### 2.1 Strike-slip Deformation

Most of the strike-slip deformation is localized along a narrow zone as attested by right-lateral offsets at a range of scale [e.g. *Hubert-Ferrari et al.,* 2002]. The largest apparent offset is made by the Kızılırmak River: between the Kargi and the Kamil releasing structures [*Barka and Kadinsky-Cade,* 1988] the river displays a 30 km long right-lateral offset [e.g. *Hubert-Ferrari et al.,* 2002; *Fraser et al.,* 2010a]. To the east and west of the Kızılırmak River, dated right-laterally offset alluvial surfaces imply a localized right-lateral motion of 18.6 +3.5/-3.3 mm/yr [Kozacı et al., 2009], and 18 ± 3.5 mm/yr [*Hubert-Ferrari et al.,* 2002] to 20.5 ± 5.5 mm/yr [*Kozacı et al.,* 2007], respectively. The fault-slip rate is similar to the GPS derived slip rate ranging from 18.7 ± 1.6 to 21.5 ± 2.1 mm/yr obtained using an local network [*Yavaşoğlu et al*., 2011] and to the InSAR derived slip rate of 21 mm/yr (14–29, 95% CI) obtained by *Hussain et al.* [2016].

There is no large geometrical discontinuity along the central NAF trace (Figure 1a). The main discontinuities are the small Kargi and the Kamil releasing step-overs that the Kızılırmak River exploits to cross the CP. These discontinuities are not large enough to arrest seismic rupture. Indeed, the Mw 7.6 Tosya earthquake on 26 November 1943 ruptured the whole central NAF from west to east over 280 km [*Barka,* 1996]. The antecedent 1668 earthquake also ruptured the NAF central bend. Paleoseismic trenching has revealed that strain along this segment is released with a relative temporal uniformity [*Fraser et al.,* 2010a].

### 2.2 Shortening and uplift in Central Pontide orogenic wedge

Around the central NAF, distributed shortening occurs uplifting the CP orogenic wedge [*Yıldırım et al.,* 2011, 2013]. Topographic swath profiles across the NAF in Figure 1c show that the corresponding a high topographic bulge centered along the NAF. The three swath profiles highlight the following characteristic and changes in topography (Figure 1c). The lowest altitudinal level corresponds to the floodplain of the Kızılırmak River that flows over 1350 km from the CAP to the Black Sea coast. Since ~2.5 Ma, the Kızılırmak River has slowly incised the CAP [*Doğan*, 2010, 2011), which was initially internally drained; it established its present course across the NAF and its outlet at the Black Sea coast around 2 Ma [*Hubert-Ferrari et al.,* 2002; *Şengör et al.,* 2005; *Yıldırım et al.,* 2011]. The CAP in the profiles is clearly identifiable by topography with a reduced relief (i.e. profile A in Figure 1c). Just to the north of the CAP, the relief increases even if the Kızılırmak baselevel stays in strain continuity with the CAP level to the south. This relief is related to the CP, a mountain chain related to the Tethyan closure that rose during the latest Cretaceous to early Tertiary [*Sengör and Yılmaz*, 1981; *Okay and Tüysüz,* 1999; *Cavazza et al.,* 2012]. The shortening was followed by a post-collisional extensional/transtensional phase [e.g. *Çinku et al.,* 2011; *Ottria et al.,* 2017]. More to the north (i.e ~ 200 km to 100 km south of the Black Sea coast), the topographic bulge of the CP range increases and reaches a maximum close to the NAF in the Ilgaz Mountains (i.e. profile B in Figure 1c). In profiles A and B, the lowest altitudinal levels are ~500 m higher than the floodplain of the Kızılırmak River sampled in profile C. Indeed, the Kızılırmak River abuts against the CP and curves eastward. The topographic bulge in profiles A and B is deeply incised by the Gerede, Devres, Gökırmak Rivers, which have carved large the V-shapped valleys.

Shortening is accommodated by different structures and reaches the Black Sea coast, where marine terraces are uplifted at a rate of 0.02 to 0.26 mm/yr [*Yıldırım et al.,* 2013b) in the Sinop peninsula, and of 0.28 ± 0.07 mm/yr farther east at the location of the Kızılırmak Delta [*Berndt et al.* 2018]. More to the south, the deformation is concentrated mostly in two distinct deformational belts (Figure 1a). The first push-up structure forms the Sinop range and is characterized by south-vergent thrusts [*Andrieux et al.,* 1995; *Yıldırım et al.,* 2011, 2013a]. There, terraces and pediments have been uplifted over the past ~350 ka at a rate of $\frac{\uparrow\downarrow}{SEP}$~0.3 mm/yr [*Yıldırım et al.,* 2013a]. The second push-up structure is centered along the NAF forming the Ilgaz Range [*Andrieux et al.,* 1995; *Yıldırım et*

133 *al.,* 2011, 2013a]. There, several compressive structures have been mapped, the main ones are located just south of
134 the NAF and bound the Tosya, Ilgaz and Cerkes sedimentary basins [*Barka,* 1984; *Over et al.,* 1993; *Andrieux et al.,*
135 1995; *Hubert-Ferrari et al.,* 2002]. These structures are seismically active as attested by the M=6.9 1951 Kursunlu
136 earthquake, which ruptured the NAF and the thrust fault to the south [*Ambraseys,* 1970]. In this second deformation
137 structure, the microseismicity study of *Karasözen et al.* [2013] has also evidenced shortening accommodated by NE-
138 SW thrust faulting and by transpression along the central NAF.
139

140 # 3 Sites studied

141

142 ## 3.1 Strath and fill terraces in the Kamil Basin

143

144 Along the Kızılırmak River, there are a number of terrace remnants standing ~70 m or higher above the present
145 floodplain [*Fraser et al.,* 2010a]. **T3** and **T2** are a set of two close strath terraces indicating river incision triggered
146 by tectonic uplift. They are located at the western end of the Kamil pull-apart (Figure 2). **T1** and **T0** are fill terraces
147 that are also observed at that location (Figure 2). Terraces were labeled according to their height with respect to the
148 Kızılırmak floodplain, **T3** being the highest one.
149

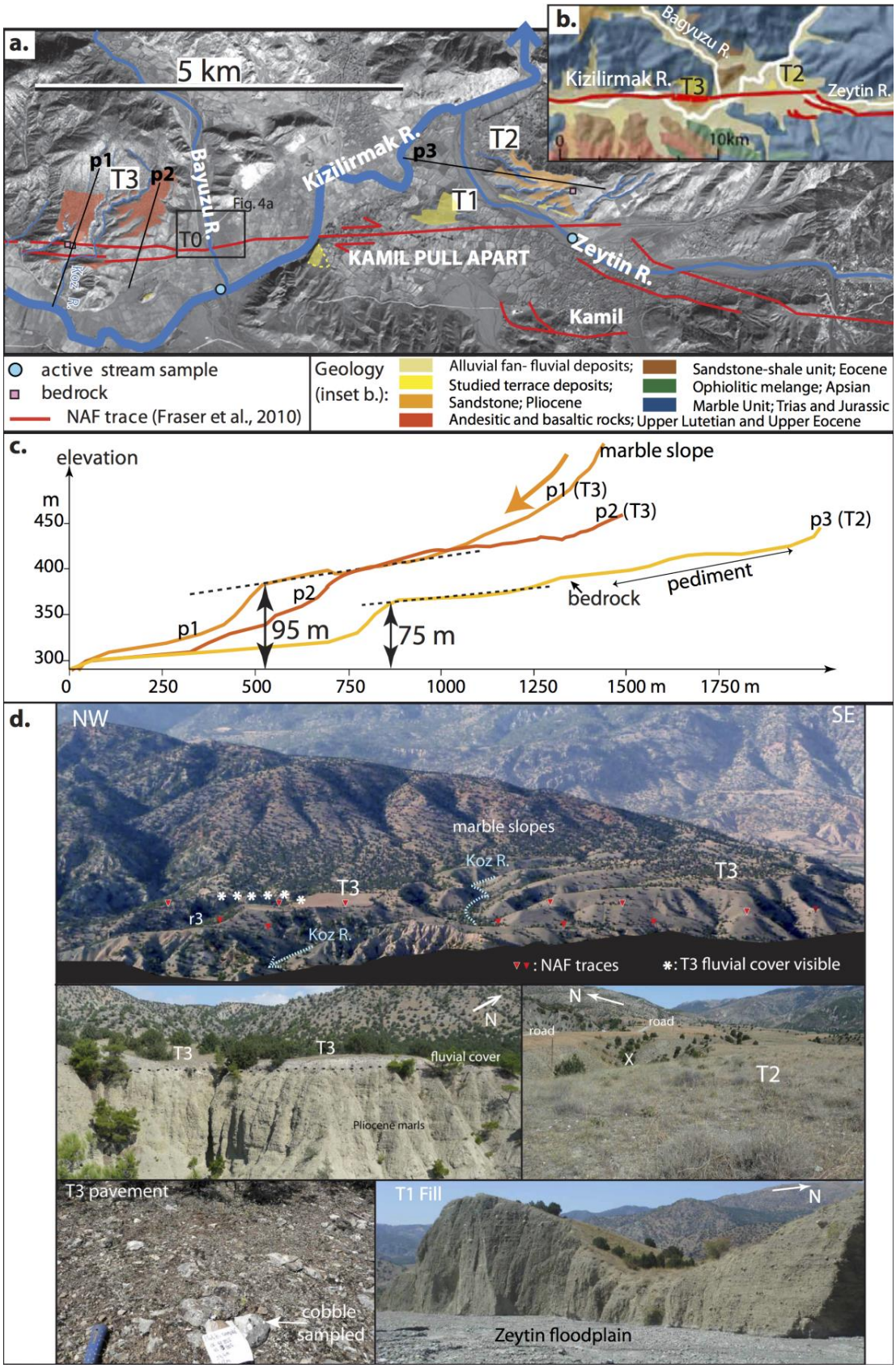
a.
5 km
p1
T3
p2
Bayuzu R.
Fig. 4a
T0
Koz R.
Kizilirmak R.
p3
T2
T1
KAMIL PULL APART
Zeytin R.
Kamil
b.
Bagyuzu R.
Kizilirmak R.
T3
T2
Zeytin R.
0
10km
active stream sample
bedrock
NAF trace (Fraser et al., 2010)
Geology
(inset b.):
Alluvial fan- fluvial deposits;
Studied terrace deposits;
Sandstone; Pliocene
Andesitic and basaltic rocks;
Sandstone-shale unit; Eocene
Ophiolitic melange; Apsian
Marble Unit; Trias and Jurassic
Upper Lutetian and Upper Eocene
c.
elevation
m
450
400
350
300
0
250
500
750
1000
1250
1500 m
1750 m
marble slope
p1 (T3)
p2 (T3)
p3 (T2)
p2
p1
95 m
75 m
bedrock
pediment
d.
NW
SE
marble slopes
Koz R.
T3
r3
Koz R.
T3
: NAF traces
: T3 fluvial cover visible
N
T3
T3
fluvial cover
Pliocene marls
N
road
road
X
T2
T3 pavement
cobble
sampled
T1 Fill
N
Zeytin floodplain

150

**Figure 2**. Maps and characteristics of terraces in Kamil Basin. **a.** Location with respect to the NAF and the river network on an Ikonos image; frame of Figure 4b is indicated. **b.** Location with respect to geology. **c.** Characteristics of strath T2 and T3 standing respectively by 75 and 95 m above the floodplain as evidenced by topographic profiles showing the T2 and T3 elevation, the connection of the western T3 surface with the hillslope and the location of bedrock outcrop at the eastern end of T2. **d**. Photographs of T1, T2 and T3. Top: view of T3; view point south of T3; location of the NAF and of the visible fluvial cover are indicated. Middle right: view of T3 carved in Pliocene marls. Middle left: T2 and its incision by a gully (label X); in the background the road built on its surface. Bottom: view of the 20-25 m thick aggradational T1 on the southern edge of T2 (Figure 3b).

**T3** is located 95 m above the Kızılırmak floodplain (Figures 2 and 3a). It is bounded to the north by a steep hillslope made of Triassic-Jurassic marbles, to the east by the Bagyuzu River and to the west by a small tributary of Kızılırmak channel. **T3** was identified on both sides of the NAF. To the south of the NAF, two **T3** remnants are bounded by steep slopes and are highly eroded. To the north of the NAF, **T3** is composed of two large surfaces with a $3.5^{o}$ slope, separated by the deep incision of the Koz River. The two surfaces show differences. The eastern **T3** surface is deeply incised and isolated because it separated from the hillslope by gullies. Its well-rounded edges show no clear natural depth profiles. Few rounded pebbles and cobbles with a diverse lithology can be found on the eastern **T3** surface. The surface bears no trace of anthropic perturbations (agricultural fields or roads) at the time of the sampling. On the opposite, the western **T3** surface is less incised and in direct continuity with slopes of marble range to the north. It is slightly more modified: its southern part has been cleared for agricultural purpose. The surface is covered by numerous poorly rounded cobbles forming a nice pavement with a uniform marble lithology identical to the upslope relief (Figure 2d). Natural depth sections are present along its southern edge. The depth profile shows a 2 to 3 m thick alluvial deposits resting upon Pliocene marls (Figures 2 and S1). The alluvial deposits are composed of thick packages of well-rounded cobbles/pebbles separated by few sandy layers.

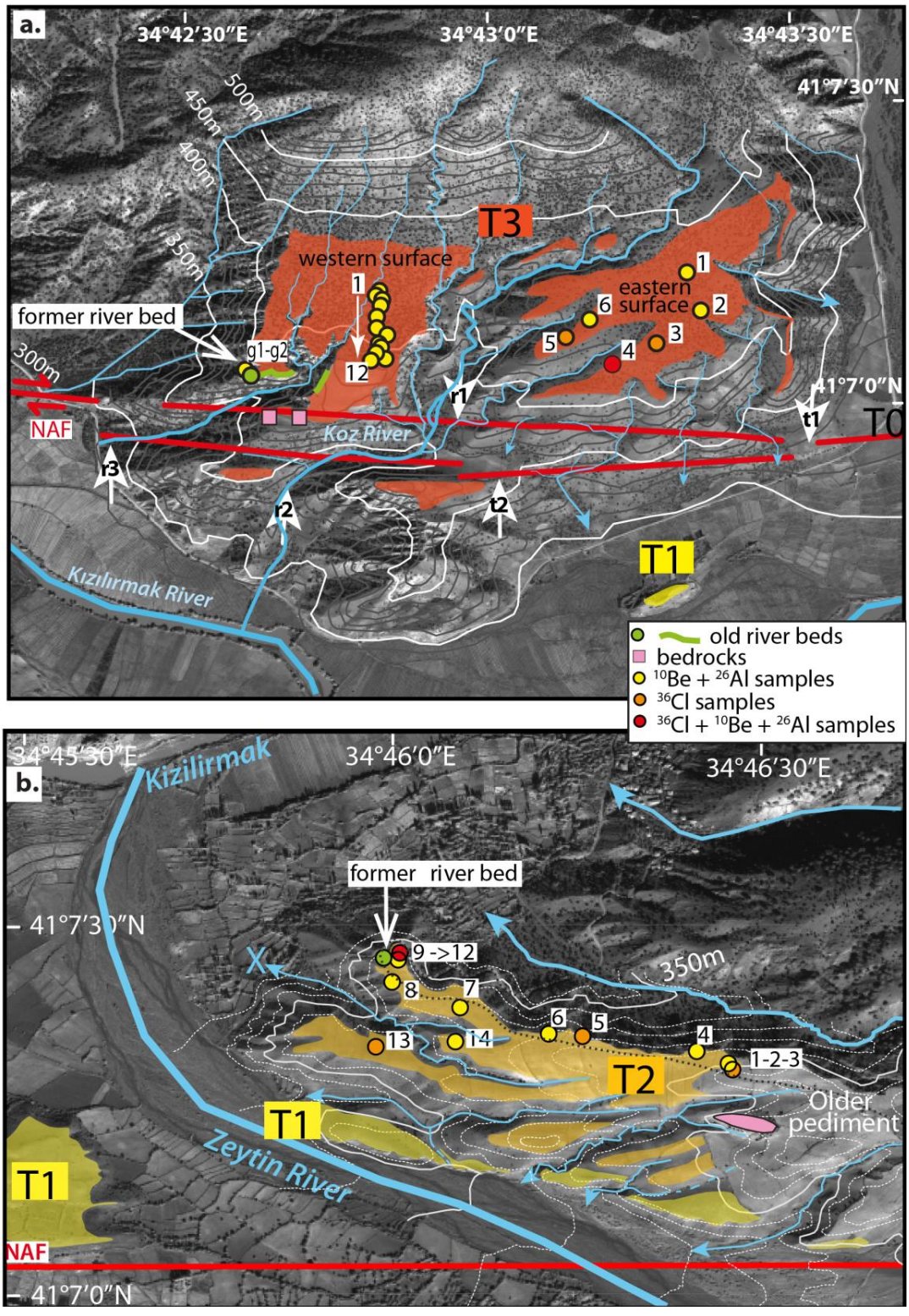


**Figure 3.** Strath terraces with topography on an Ikonos image and location of cobbles samples for cosmogenic nuclide dating **a**. T3 with arrows indicating the offset of the Koz River (r1 to r2) separating the western and the eastern T3 surfaces, and the offset of the T3 edges (t1 to t2) that

matches a larger offset of the Koz River (r1 to r3). **b**. T2 limited to the east by a marble bedrock (pink); gully labeled X in Figure 2d is indicated. The fill terrace T1 is mapped.

**T2** is located 75 m above the Kızılırmak River (Figures 2 and 3b). It is limited to the west by the Kızılırmak and to the north by one of its tributary. To the east, **T2** is connected to a smooth pediment surface inclined towards its surface. T2 and pediment surface are separated by gullies and by a marble bedrock outcrop. To the south, **T2** is bounded by **T1** a younger very homogenous aggradational fill terrace. The **T2** surface is deeply incised by gullies and is covered by cobbles having various lithologies. **T2** is more modified than **T3**: a road was built along its entire length and the surface was cultivated. Aligned reworked cobbles and boulders form the edges of former fields. Along the road cut at **T2** western end, a depth-profile evidenced a 1.30 m thick fluvial deposit composed of polygenic pebbles and channels filled of clayed sand with visible cross-bedding structures (location in Figure 3b and section in Figure S1). At that location, a debris flow deposit locally covers the **T2** surface.

The **T1** thick aggradation fill is visible mostly near the intersection of the Zeytin and the Kızılırmak Rivers, though a small T1 remnant is also visible south of **T3** (Figures 2 and 3b). The homogeneous ~20 to 25 m thick aggradational package shows no major discontinuity and no paleosoil formation. These observations suggest that it was deposited over a short period of time, after the incision and abandonment of **T2** and **T3**. T1 is also visible in the Kargı Basin located 35 km more to the west (Figure 1a).

### 3.2 Deformation pattern

Fault mapping done by *Fraser et al.* [2010a] reveals the occurrence of a ~1 km pull-apart basin at the confluence between the Zeytin and the Kızılırmak Rivers (Figure 2a). West and east of pull-apart, the NAF is very linear and continuous. Across **T3**, it displays two parallel strands marked by numerous geomorphic features (Figures 2 and 3a). To the east of the Koz River, the two strands are identified by small stream offsets and captures, upslope facing scarps and a small flat pull-apart (Figure 3a). The southern strand is visible in section in the Koz River. To the west of the Koz River, the northern strand deformed **T3** forming a 1m high north facing scarp and the bedrock outcrops (pink squares in Figures 2a and 3a); the southern strand is marked by a side-hill bench. East of **T3**, a single NAF active trace is evidenced across the Baygyuzu floodplain and **T0** a low terrace (Figures 2a and 4a). Farther east, the NAF could not be precisely mapped because of intense farming activity and high sedimentation/erosion rates. Local people pointed traces of the 1943 fault rupture [*Frasers et al.,* 2010a]. On the other side of the Kızılırmak floodplain, the NAF runs to the south of the present Zeytin floodplain and bounds to the south a remnant of **T1** (Figure 3b). Right-lateral offsets across **T3** and the Baygyuzu floodplain are described in the following as they provide information regarding the NAF deformation pattern.

Across **T3**, two large cumulated right-lateral offsets are evidenced. The most obvious one is the apparent ~370 m offset of the Koz River indicated in Figure 3a by arrow r1 for the catchment north of the NAF incising **T3** and by arrow r2 for the narrow channel south of the NAF. However, the right-lateral offset of the Koz River is probably larger: south of the NAF, the initial river channel was probably the one located farther west (arrow r3, Figure 3a). The r3 channel is larger that r2, but it has a smaller catchment north of the NAF insufficient to generate the stream power necessary to carve its deep and wide channel. This r1-r3 offset is consistent with the 750 m right-laterally offset of the **T3** eastern edge indicated by white arrows t1 and t2 in Figure 3a. Indeed, the original **T3** surface can be reconstruct using a 750 m backward left-lateral translation. As a result, the **T3** remnants and the r3 channel, south of the NAF fall in front of the eastern **T3** surface and the Koz River north of the NAF, respectively (Figure 3a). The morphology therefore suggests a minimal cumulative displacement of 750 m of an incision phase posterior to the **T3** bevelling.

East of **T3**, on both sides of the Baygyuzu River, **T0** is also deformed (Figure 4). Its surface is farmed and stands ~3m above the ~100 to 200 m wide floodplain (Figure 4a and 4d). It is crossed by a fresh 0.5 to 1m a continuous south-facing scarp (Figure 4c). Close to the river, **T0'** an additional inset paired terrace stands 1 to 2 m above the riverbed (Figures 4a and 4d). Theodolite profiles shows that the floodplain is warped (Figure 4d). On the western side of the river, the **T0**/**T0'** riser is protected from active river erosion and records a cumulated right-laterally offset of 14±2m based on theodolite measurements (Figure 4b). **T0'** shows a possible right-laterally offset of 2 m, identical to the 1943 earthquake slip documented at that location [*Barka*, 1996]. The low slip in the Kamil area during the

1943 earthquake was also documented by a water channel offset in the nearby Alibey village located 12 km East of Kamil (Figure S2).

Four ~1m deep trenches were excavated to constrain the stratigraphy, deformation and age of the terraces (Figures 4b, 4d, and 4e). Tr2 in **T0** is the reference trench Tr2 dug across the fault scarp; Tr1, Tr3 and Tr4 were dug in the risers. In all trenches, the bottom unit (unit 4 in Tr2, unit 3 in Tr1, unit 2 in Tr3 and Tr4) contains more than 25% of pebbles/cobbles and a significant sand fraction (Figures 4d and 4e). This coarse grain-size distribution is similar to the present floodplain deposit. This unit is overlain by finer grained units with a sharp contact in **T0** (Tr1, Tr2, Tr4) and a gradational contact in **T0'** (Tr3). The transition between the pebbly bottom unit and the overlying finer grained units is interpreted to correspond to the time at which the terraces were incised. The finer grained units are interpreted to result from exceptional flood events and from deflation, which would rework fine sands from the floodplain and transport them on the terrace surface. In **T0**, the large variation in grain-size of the upper most units between the different trenches is supposed to be related mostly to anthropogenic modifications for agricultural purpose: cobbles were removed from the main surface (i.e Tr2) and stored on its edges (i.e. Tr1).

In Tr2, the top unit 1 and the bottom unit 4 are folded across the scarp (Figure 4e); folding of unit 4 is about twice more important than the warping of unit 1, which implies than the scarp results from at least two deformational episodes. No distinct fault trace could be identified due to the restricted depth of the Tr2 trench and to the difficulty of identifying fault terminations in gravels. Two additional units are present on the down-through side of the scarp: unit 2, a coarse wedge composed of 15 % pebbles in a fine sandy matrix, overlying unit 3, a finer grained unit composed of coarse sands with laminations. We interpreted unit 2 as a colluvial wedge resulting from the collapse of a fault scarp (free face) after an earthquake, and unit 3 as an overbanked deposit on top of the river gravels (i.e. unit 4). The base of the colluvial wedge (unit 2) is therefore interpreted as an earthquake event horizon.

The deposition chronology is constrained by radiocarbon dating. In Tr3 (**T0'**), the wood sample at the trench bottom (i.e 85 cm) gave an uncalibrated age of 270±40 yrs and a calibrated age with an 86% probability of occurrence during the 1486-1676 A.D. period (Figure 4d). In Tr2 (**T0**), two large wood samples were collected at the base of unit 2, the colluvial wedge (Figure 4e) and would have been trapped during the scarp collapse. The uncalibrated ages of 30±50yrs BP and 80±30yrs B.P., and the respective calibrated ages imply a 70.5% probability of occurrence during the 1805-1931A.D. period and a 70.5% probability of occurrence during the 1810-1926 A.D. period. A small sample was collected at the boundary between the overbank sandy unit 3 and the river gravel unit 4 to constrain the incision age of T0. We obtain an uncalibrated age of 350±40yrs B.P. and a calibrated age implying a 95% probability of occurrence during the 1455-1638 AD interval.

The stratigraphy and the calibrated ages suggest that the terrace history is in relation with the two last earthquakes rupturing the central NAF in 1943 A.D. and 1668 A.D. [*Barka*, 1996]. **T0** has been incised and abandoned shortly after the penultimate AD 1668. In this scenario, the top of the bottom unit 4 in T0 is the 1668 A.D. event horizon. Tr2 stratigraphy and dating also imply that the 14 m **T0**/**T0'** riser offset results from the 1943 A.D. and 1668 A.D. cumulated ruptures. The cumulated displacement is similar to the 15.5 m of right-lateral displacement of large old water canal built before the 1943 earthquake in the village of Alibey, located 12 km to the east of the investigated site (see Figure S2). The ~2m historical offsets related to the 1943 earthquake in the Kamil area [*Barka,* 1996] imply that the 1668 A.D. surface slip was greater than 10 m. This is in agreement with the larger magnitude of the 1668 A.D. earthquake and the conclusions of *Fraser et al.* [2010a, 2010b]. They inferred that the displacement per event along the central NAF is variable between seismic cycles, based on a paleoseismic trenching study located east of Kamil pull-apart.

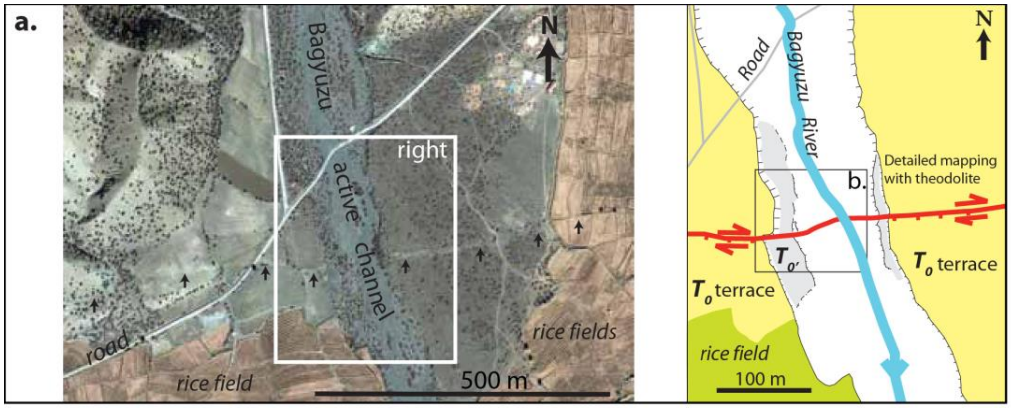


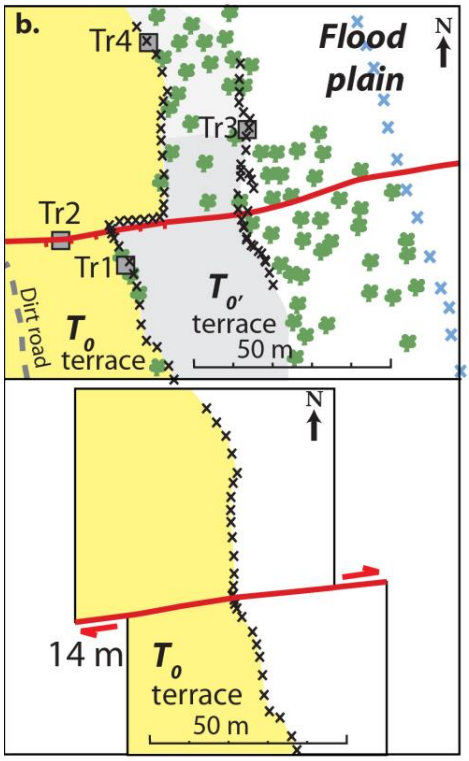


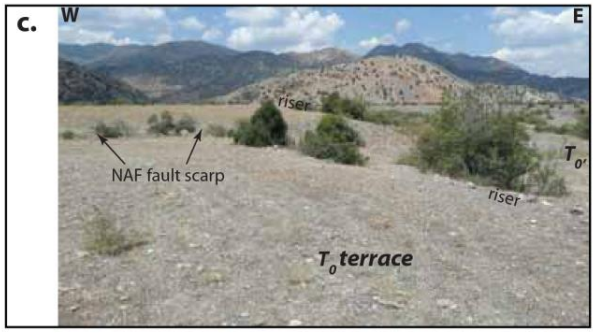


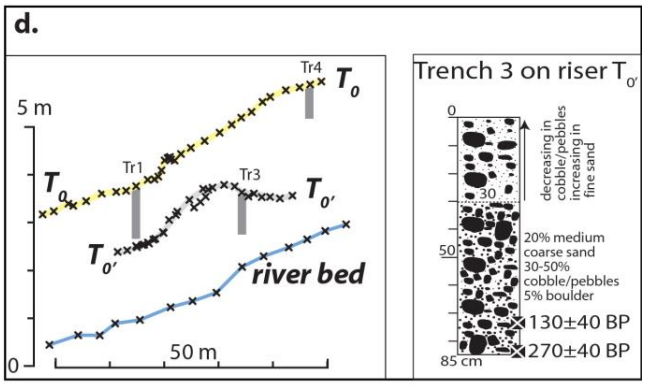


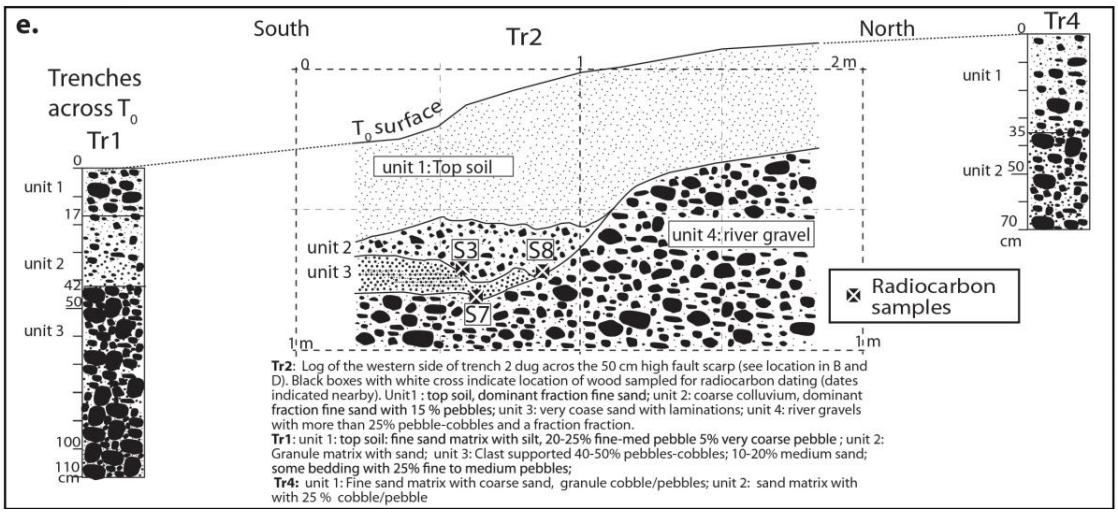


**Tr2**: Log of the western side of trench 2 dug acros the 50 cm high fault scarp (see location in B and D). Black boxes with white cross indicate location of wood sampled for radiocarbon dating (dates indicated nearby). Unit1 : top soil, dominant fraction fine sand; unit 2: coarse colluvium, dominant fraction fine sand with 15 % pebbles; unit 3: very coase sand with laminations; unit 4: river gravels with more than 25% pebble-cobbles and a fraction fraction.
**Tr1**: unit 1: top soil: fine sand matrix with silt, 20-25% fine-med pebble 5% very coarse pebble ; unit 2: Granule matrix with sand; unit 3: Clast supported 40-50% pebbles-cobbles; 10-20% medium sand; some bedding with 25% fine to medium pebbles;
**Tr4:** unit 1: Fine sand matrix with coarse sand, granule cobble/pebbles; unit 2: sand matrix with with 25 % cobble/pebble

280

**Figure 4**. T0 and T0' offset by the NAF. **a**. Left: Ikonos image of the site, showing the NAF cutting the Bagyuzu active river bed and older alluvial deposits; fault scarp facing south marked by black arrows; box indicates location of figure to the right. Right: geomorphological map with T0 in yellow and T0' in grey; box indicates location of Figure 4b. **b**. Top: map of T0 and T0' on the river western side. Risers and riverbed were measured in the field with a theodolite (i.e. crosses: individual measurements); grey squares indicate trench locations. Bottom: reconstruction of a straight T0 riser using a back left-lateral motion of 14 m; T0/T0' riser is offset by about 2 m. **c**. Photo of the offset T0/T0' riser and of the fault scarp. **d**. Left: theodolite profiles projected north showing T0 and T0' relative heights with respect to the riverbed; trenches location indicated. Right: Tr3 log in T0' riser and $^{14}C$ ages obtained. **e**. Trenches across T0. Middle: log of the Tr2 western side across the 50 cm high scarp; black boxes with white cross indicate location of wood samples for radiocarbon dating (dates indicated in the text). Left: Tr1 log. Right: Tr4 log.

### 3.3 The Kızılırmak watersheds studied

To evaluate the denudation of the CP Range, we seek to obtain catchment-averaged denudation rates using cosmogenic nuclide concentrations. We focus on the Kızılırmak catchment directly affected by the NAF within the CP orogenic wedge, and sampled 9 river catchments: the Kızılırmak River (present-day and past river beds), three of its main tributaries, the Devres, the Zeytin and the Baygyuzu Rivers, and five subparallel tributaries of the Devres River (Figure 5, Text S1).

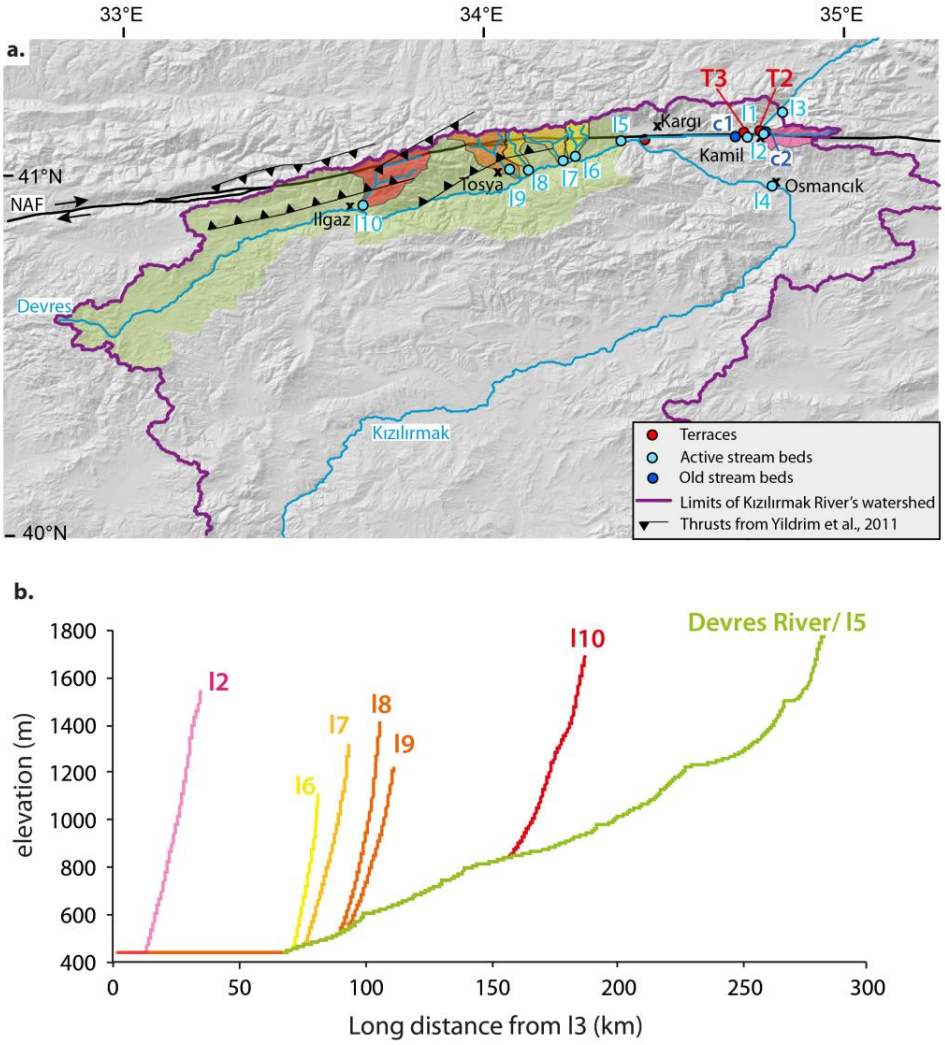


**Figure 5**. Studied watershed for erosion rates. **a**. Location of the river sampled for cosmogenic-based erosion rates. The studied catchments are outlined with different color. **b**. River profiles of some studied catchments.

# 4 Method

## 4.1 Cosmogenic-based erosion rates

Cosmogenic nuclide concentrations in river sediments were used to infer catchement-average denudation rates. We use the sandy fraction of 11 active riverbeds (Figure 5) to infer erosion rates over the Holocene, and two former river beds in T2 and T3 (Figure 3) to try to obtain a rate over the last glacial period. Additional details about regarding sampling and method are included as supplemental materials (Text S2, Figure S3). Sample locations are included in Table S1.

### 4.2 Terrestrial cosmogenic nuclide exposure dating

A key issue regarding tectonogeomorphology is the ability to constrain the age of deformed geomorphic markers like alluvial terraces, rockfalls and landslides [e.g. *Tapponnier et al.,* 2001]. This is possible by measuring terrestrial comogenic nuclides. For the studied Kızılırmak terraces, we used a combination of three radionuclides $^{10}$Be, $^{26}$Al, and $^{36}$Cl to constrain their exposure history. Sample locations are given in Table S1, and results in Tables 2 and 3. Details about the materials, methods and specific sampling strategy for minimizing the erosion bias can be found as supplemental materials (Text S2, Figures S2 and S3).

The sample ages are represented using density probability function to access the data dispersion and possible pluri-modal distribution (Figure 6). Following *Brown et al.* [2005], a pluri-modal distribution may indicate post-depositional reworking and in that case, the oldest ages would represent the age of the surface. In other cases, a large dispersion may represent a variable inheritance, the youngest ages would have the smallest inheritance and would be representative of the terrace abandonment [e.g. *Meriaux et al.,* 2005; *Le Dortz et al.,* 2009]. In the present paper, we discussed the geomorphologic processes at play on the terraces to interpret exposure dates [*Applegate et al.,* 2012], and did not follow directly the previous interpretations.

## 5 Results and interpretation

### 5.1 Denudation Rates

The erosion rates obtained (Table 1) are generally higher than the average worldwide drainage erosion rate (i.e. 218 m/Ma in *Portenga et al.* [2011]).

Regarding the Kızılırmak River, its average erosion rate is weakly constrained to 380 m/Ma, but our data imply a minimum erosion rate of 160 m/Ma, which is 3 times higher than the 50-60 m/Ma inferred on the CAP [*Çiner et al.,* 2015]. The low erosion rate on the plateau might be related to its increase aridity with respect to its border. The CAP has an average rainfall of 200 to 600 mm/yr whereas the CP receives an average rainfall between 300 and 1200 mm/yr. The compilation of $^{10}$Be erosion rate data shows that arid region drainage basins tend to erode more slowly than others [*Portenga et al.,* 2011]. However, *Von Blanckenburg* [2006] that denudation rate in basins having a similar granitic geology strongly falls only below a rainfall threshold of 200 mm/yr. So the more arid climate of the CAP may not be the cause of its lower denudation rate. Another factor is tectonics. The CP are active uplifting whereas the CAP is mostly stable [e.g. Reilinger et al., 2006], and denudation is correlated with tectonics [*Von Blanckenburg,* 2006; *Portenga et al.,* 2011] because of the strong control of tectonics over rock weathering [*Edmont and Huh,* 1997]. So we infer that the higher denudation rates in the CP compared to the CAP are linked to its active deformation and its related higher relief.

The catchments in the CP Range have an average $^{10}$Be computed rate of 395 mm/ka, which is of the same magnitude as the Kızılırmak River (Table 1). Catchments show a large range of erosion rates. The highest rates occur in the N-S oriented catchments directly affected by thrust faulting: i.e L1, Baygyuru (482±120m/Ma), L6 (710±170 m/Ma) and L8 (324±67 m/Ma) across the Tosya Basin and L10 (514±191 m/Ma) across the Ilgaz Basin. L6, at the eastern end of the Tosya Basin, also has an headwater located in easily erodible ophiolitic rocks and has one of the steepest river gradients (Figure 5). The lowest rate concerns the Zeytin catchment, l2 (134±36 m/Ma). It may be surprising given that it strikes along the NAF, which would have damage rocks close to its main strand potentially enhancing erosion. Its lower erosion rate might be related to the strong perturbation induced by the large active landslide affecting its catchment and to the absence of active thrusts. The east-west oriented Devres River shows a denudation rate of 220 mm/ka that is much lower than its northern tributaries. Indeed, the northern part of the Devres catchment (i.e Tosya and Ilgaz Basins) is crossed by the NAF and by active thrust and folds, and is limited by the high peaks of the Ilgaz Mountains (Figures 1 and 5). The Devres catchment has a lower denudation rate than the tributaries sampling this actively uplifting range, because it has a lower slope on average and is also sampling lower and less actively deforming ranges. Our results thus suggest a strong tectonic control of the denudation rates in CP and in Anatolia, as documented elsewhere in the geological record (i.e., Armitage et al., 2011).

$^{26}$Al measurements obtained from two former river beds in T2 and T3 (Figure 3 and S1; Table 1 and S1) when corrected of post-depositional production of $^{26}$Al gave very low concentrations ranging from 27 000 at/g to 10 000 at/g. These measurements suggest that the denudation rates during the Last glacial period were larger than during the Holocene. Higher denudation rates may be related to an increase in physical weathering in the mountainous regions during cold period (e.g. Hales and Roering, 2007; Matsuoka, 2008; Fuller et al., 2009; D'Arcy et al., 2017). This mechanism was suggested in particular regarding in the carbonate mountainous regions in the Mediterranean area (i.e. Benedetti et al., 2002; Tucker et al., 2011).

## 5.2 Ages of T3 and T2 with no erosion and inheritance

On **T3**, we distinguished the eastern surface from the western one (Figure 3a), because they show a completely different age pattern (Figure 6). On the **eastern T3** surface, three $^{26}$Al/$^{10}$Be (T3-3 to 5) and four $^{36}$Cl ages (T3-1, 2, 4, 6) were obtained (Figure 6, Tables 1, 3, S1 and S4). The $^{10}$Be ages obtained (T3-3: 99±9 ka; T3-4: 64±7 ka; T3-5: 71±7ka) are clustered and are concordant with $^{26}$Al ages (Table 1). The four $^{36}$Cl ages (T3-1: 102±12ka; T3-2: 112±13 ka; T3-4: 72±8 ka; T3-6: 78±9 ka; Table 2) are also compatible with the $^{10}$Be ages.

On the **western T3** surface, we obtained fourteen $^{36}$Cl ages (T3W-1 to 12, T3W-g1, g2; Figures 3 and 6, Tables 2, S1 and S4). No $^{10}$Be/$^{26}$Al exposure age sample was obtained because no quartz rich cobbles were found on the surface. All exposure ages are younger than on the **eastern T3** surface (Figure 6). Regarding the twelve samples taken along a north-south profile in the most preserved central part of the terrace (T3W-1 to 12), their ages get younger upstream toward the hillslope. Representing the sample ages using probability functions, we identify two clusters, one around 22 ka for samples located close to the hillslope, and a secondary one around 40-50 ka for the samples located father south (Figure 6). The samples taken near the steep eroded T3 edge (T3W-g1, g2) have ages of 28±3 ka and 11±1ka (Table 2). This later young age is attributed to local enhanced erosion near the terrace edge (see Figure S1).

On **T2**, fourteen samples (T2-1 to 14; Tables 1, 2, S1 and S4) were processed given the complex natural and human processes that could have modified it (Figure 3b). Among them, four samples were located close to T2 edge where the road cut evidenced a debris flow on top of the terrace alluvial deposit (T2-9 to 12). Excluding these samples in a first step, the three $^{26}$Al/$^{10}$Be ages obtained show a wide spread (T2-2: 31±3 ka; T2-5: 20 ±2ka; T2-13: 58±5ka; Figure 6; Table 1); the eight $^{36}$Cl ages obtained show a similar spread from to 27±3 ka to 107±12 ka (Figure 6, Table 2). When we represent the sample ages using probability functions, we evidenced two clustered centered respectively on 25 and 40 ka (Figure 6). The four surface samples from the debris flow also show a wide age range from 31±3 ka to 85±8 ka (T2-9 to 12 in Tables 1, 2). The cosmogenic ages of the debris flow imply that the oldest exposure age of the alluvial surface (T2-4: 107±12 ka) is an outlier, and it was excluded. The age spread in the debris flow is related to the fact that it reworked already exposed cobbles with a significant inheritance. Only the youngest samples (T2-9: 31±3 ka, T2-12: 34±4ka and 45±5ka, Tables 1 and 2) were used to infer its emplacement that would have occurred around 30-45 ka. We used these ages as a constraint for **T2** that must be older than 45 ka.

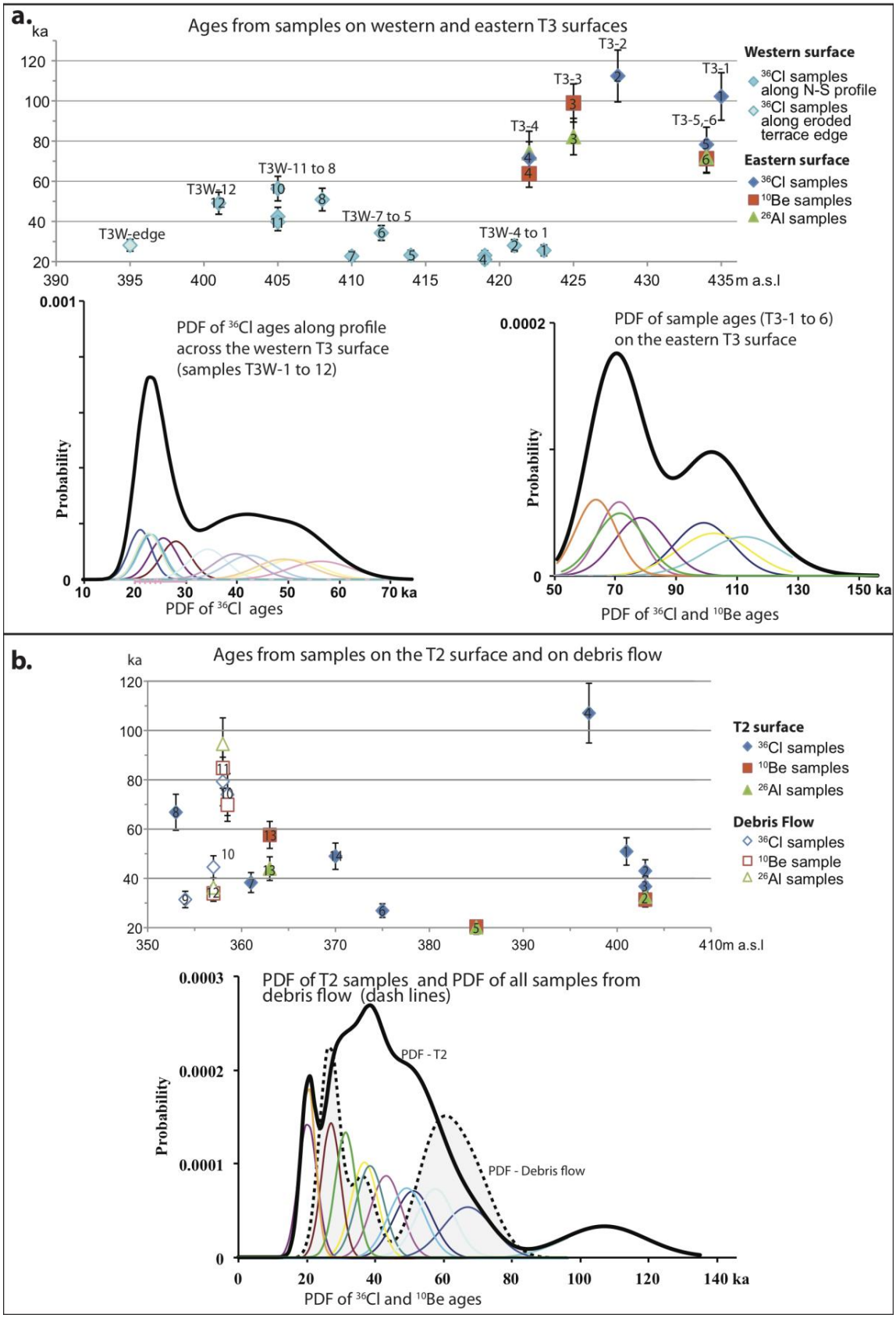
a.
Ages from samples on western and eastern T3 surfaces
ka
Western surface
36Cl samples along N-S profile
36Cl samples along eroded terrace edge
Eastern surface
36Cl samples
10Be samples
26Al samples
T3-1
T3-2
T3-3
T3-4
T3-5,-6
T3W-edge
T3W-12
T3W-11 to 8
T3W-7 to 5
T3W-4 to 1
m a.s.l
PDF of 36Cl ages along profile across the western T3 surface (samples T3W-1 to 12)
Probability
PDF of 36Cl ages
PDF of sample ages (T3-1 to 6) on the eastern T3 surface
PDF of 36Cl and 10Be ages
b.
Ages from samples on the T2 surface and on debris flow
T2 surface
36Cl samples
10Be samples
26Al samples
Debris Flow
36Cl samples
10Be sample
26Al samples
m a.s.l
PDF of T2 samples and PDF of all samples from debris flow (dash lines)
PDF - T2
PDF - Debris flow
Probability
PDF of 36Cl and 10Be ages

410

**Figure 6.** T3 and T2 cosmogenic exposure ages. **a.** Top: T3 exposure ages represented versus elevation above sea level (a.s.l.). Bottom right, probability density function of $^{36}$Cl exposure ages for samples T3W-1 to T3W-12 following a north-south profile on the western surface. Bottom left: probability density function of $^{36}$Cl and $^{10}$Be exposure ages for all samples the eastern T3 surface. **b**. Top: T2 exposure ages represented versus elevation above sea level (a.s.l.). Bottom, probability density function of exposure ages. Samples corresponding to the debris flow (T2-9 to 12) are identified.

## 5.3 Evaluation of Erosion Rates and inheritance on T2 and T3

Possible corrections related to erosion rates were evaluated. Erosion reduces the cosmogenic isotope concentrations giving rise to ages that are too young. Several constraints could be inferred. First, we have developed a sampling strategy to minimize this bias (see Text S2). Second, we considered that the erosion rates on the inner part of the terraces, particularly **T3**, were likely to an order of magnitude smaller than the obtained averaged denudation-rate around 200m/Ma obtained using river sand. Third, we inferred that $^{36}$Cl ages are not in equilibrium because of their agreement with Be-Al ages, and thus computed a maximum erosion rate of 6 mm/yr. Finally, *Yıldırım et al.* [2013] based on $^{10}$Be depth profile on a terrace inferred a possible erosion rate of 1 mm/ka in the nearby Gökırmak catchment. All these elements point to a low to negligible erosion rate of the inner part of the terraces.

We also critically assess erosional processes on the terraces. The former Kızılırmak alluvial deposits visible in sections across **T2** and **T3** are mostly composed of cobbles with few coarse sand layers. The main erosion processes on these surfaces after their incision and abandonment would be driven by overland flow and deflation. Large overland flows could be erosive particularly during cold and arid glacial periods with a restricted vegetation cover, but cobbles are still likely to have a long residence on the inner flat part of the terrace. Deflation would affect only the finest particles, and concentrate the cobbles at the surface. This process would have a relative minor impact because of the original large grain-size of the alluvial deposits as evidenced in the depth section (Figure S1). The erosion rate by these two combined processes is thus likely to be minimal. On **T2**, cultivation has triggered the exhumation of buried cobbles and may have increased the erosion rate of the finer particles, but we are lacking any way to quantify these parameters. We thus rely more on the exposure ages of **T3**.

The prior exposure is the other important bias, cobbles could have gained an initial concentration before their deposition on the terrace. *Yıldırım et al.* [2013] evaluated in the nearby Gökırmak catchment possible inherited $^{10}$Be concentrations ranging from 140 000 to 40 000 atoms.g$^{-1}$. Similarly, *Çiner et al.* [2015] evaluated the inherited concentration in Kızılırmak terraces in the CAP between 0 and 15-25 x $10^3$ atoms.g-1 on a 160±30 ka terrace. Another way to assess the presence of inherited nuclides is to date the active riverbed [e.g. *Hetzel et al.,* 2006]. We obtained $^{10}$Be concentration ranging from 10 000 to 50 000 atoms.g$^{-1}$ in riverbeds. To evaluate the most adequate inheritance, we tested different inheritance scenario within the 10 000 to 50 000 atoms.g$^{-1}$ range using the few radionuclide concentrations obtained at depth in **T2** and **T3** (see Figure S1). The two profiles could be fitted with no inheritance or with a small one of 10 000 atoms.g$^{-1}$.

We thus considered that inheritance is negligible, and that most of the age spread is related to other specific geomorphological or anthropic processes further discussed in the following. We choose not to apply any systematic corrections for erosion and prior exposition.

## 5.4 Terrace ages, age spread and the inferred frost-cracking process

The exposure ages for the two surfaces show a broad spread (Figure 9), but the large number of exposure ages allows for identification of probable geomorphological processes responsible for the sprawl. The **T3** surface, which is the most preserved regarding anthropic modifications, shows the clearest pattern. The **T3** cobbles located west and east of the Koz River belong to the same surface (Figure 2), but have different exposure ages (Figure 6a). So different geomorphological processes were at play on these surfaces. The younger exposure ages on the **western T3**

surface are thus interpreted to reflect hillslope processes during the Glacial Period, posterior to the terrace bevelling and entrenchment.

During cold intervals, a dominant erosional process on bare marble hillslopes of the CP range would be frost cracking [*Anderson et al.,* 2013]. This specific process at play during the Glacial Period was evidenced around the Mediterranean [*Tucker et al.,* 2011]. It leads to a larger degradation of carbonate slopes during the Glacial Period compared to the Holocene [e.g., *Armijo et al.,* 1992; *Piccardi et al.,* 1999; *Morewood and Roberts,* 2000]. Marbles samples along the north-south profile on the **western T3** surface are interpreted to come from the hillslope by frost cracking.

The intensity of frost cracking depends on two main variables: first, the time spent in the frost cracking window (ranging from -8 to -4$^{o}$C) and second, the water availability directly linked to Winter/Spring precipitation [*Anderson and Anderson*, 2010]. A cold and humid climate would be much more favorable than a cold and dry one. High-resolution pollen data from the southern Black Sea cores record vegetation changes in the CP [*Mudie et al.,* 2007; *Shumilovskikh et al.,* 2012, 2013 and 2014] and attest for the occurrence of large changes in temperature and humidity implying that frost cracking would not be a steady phenomena [*Anderson et al.,* 2013]. The two age clusters at 23-2+3 ka and between 40 to 55 ka on the **western T3** surface correspond to the two coldest intervals during the last 135 ka in the CP [see *Badertscher et al.,* 2011], and particularly to the two more humid periods identified using pollen data around 45-54 ka and 20-28 ka in the CP [*Langgut et al.,* 2011; *Shumilovskikh et al.,* 2014]. These more humid phases correspond to glacial advances in Turkey. The first one fits the 53-44 ka glacial advance [*Reber et al.,* 2014] in Eastern Black Sea Mountains in Turkey, and the second one, the better known Last Glacial Maximum (LGM) advance in Turkey. The LGM in Turkey is characterized by cooler temperature and a doubling in precipitation at 22±4ka in comparison with the previous period [*Akçar et al.,* 2014; *Reber et al.,* 2014].

The age distribution for the **western T3** surface can thus be simply related to the fact that the surface acts as a pediment in direct connection with a carbonate hillslope (Figure 7). Periodic frost cracking on the hillslope brings new carbonate cobbles on its surface, the last episode being the LGM. Cobbles originating from frost cracking would then be transported away from the slope when large overland flow occurs. So older marble cobbles would be found farther away from the slope. This geomorphological scenario is consistent with the exposure ages obtained along the profile across **T3** (T3W-1 to 12; Figure 3a): many LGM carbonate cobbles are found near the hilslope and there is a trend toward older ages away from the hillslope (Figure 6a). It also provides an explanation for the numerous carbonate cobbles present on the **western T3** surface forming a pavement (Figure 2e) and the few older cobbles with a mixed lithology found on the **eastern T3** surface. The **eastern** and **western T3** surfaces have different histories because the **eastern T3** surface is separated from the hillslope by a gully system forming the head catchment of the Koz River (Figure 3a), so the eastern surface is disconnected from the hillslope. **T3** abandonment and incision can thus only be inferred by using samples on the eastern surface; an abandonment age of 85±15ka for **T3** is thus computed by averaging its $^{10}$Be and $^{36}$Cl exposure ages. **T3** age is compatible with $^{10}$Be and $^{326}$Al exposure ages at depth in **T3** (Table 1; Figure S1).

On **T2**, two main processes are inferred. First, frost-cracking is likely to be present because part of the **T2** surface is in continuity with a pediment and the carbonate bedrock, which itself is connected to carbonate slopes (Figures 2c and 3b). Indeed $^{36}$Cl ages belonging to the two main frost-cracking periods, LGM (T2-6: 27±3 ka) and 40 to 55 ka (T2-1: 51±6ka, T2-7: 38±4ka, T2-14: 49±5ka), are also present on the **T2** surface Figure 6b). Second, human ploughing, which leads to younger exposure ages for exhumed cobbles can be a bias, even if we sampled away from visible fields and selected cobbles with a large alteration ring. Given this two potential bias, we consider that samples most representative of the terrace age should have the oldest ages and should come from an isolated terrace remnant. Sample T2-8 (66.8±7.3 ka) is thus considered the best to represent the terrace age because it is the oldest exposure age and it comes from a surface surrounded by deep gullies. This inference is consistent with the fact that T2 bevelling must be (1) older than the debris flow emplaced around 30-45 ka, and (2) younger than **T3**. Finally this age is also coherent with cosmogenic concentrations we have at depth in **T2** (Table 1; Figure S1).

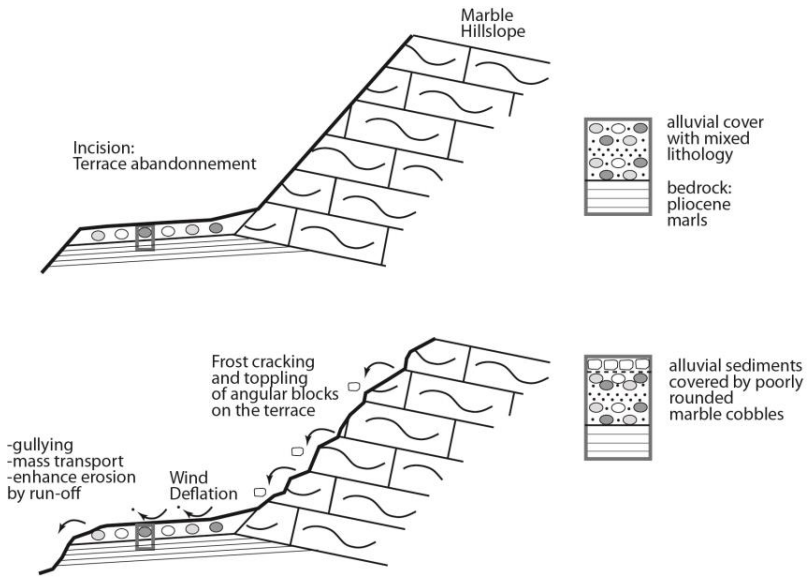


**Figure 7.** Sketch displaying the geomorphological processes at play in a cross-section since terraces incision and abandonment (top diagram): the terrace surface acts as a pediment (bottom diagram) where new marble cobbles are supplied by frost cracking by the hillslope, and are in transit on the surface; on the right, typical sedimentary sections across the terraces.

## 6 Discussion

### 6.1 Terrace formation, incision and possible climate-related factors

The 85±15 ka age of **T3** age concordant with ages of strath terraces (81±8 ka and 99±8 ka $^{10}$Be ages and 78±7 ka $^{36}$Cl age) and pediments (70±7 ka $^{21}$Ne age) in the Gökırmak River, a tributary of the Kızılırmak River [*Yıldırım et al.,* 2013a] (Figure 8). More to the west, a strath terrace with an 88±5.1 ka age was also mapped along the Filyos River [*McClain et al.,* 2017] (Figure 1a). **T3** in Kamil thus results from regional episode of strath planation that took place during MIS 5a/b. The **T3** formation is also broadly coincident with the abrupt replacement of mixed forest by steppe species in the eastern Mediterranean area during MIS 5a [*Litt et al.,* 2014]. The vegetation and climatic changes are likely to have increased the sediment supply in the CP, as evidenced by the high erosion rates obtained from the Kızılırmak paleochannels. High sediment supply would have lead to the strath planation in Kamil and more to the north or to the west in the Gökırmak and Filyos catchment, respectively.

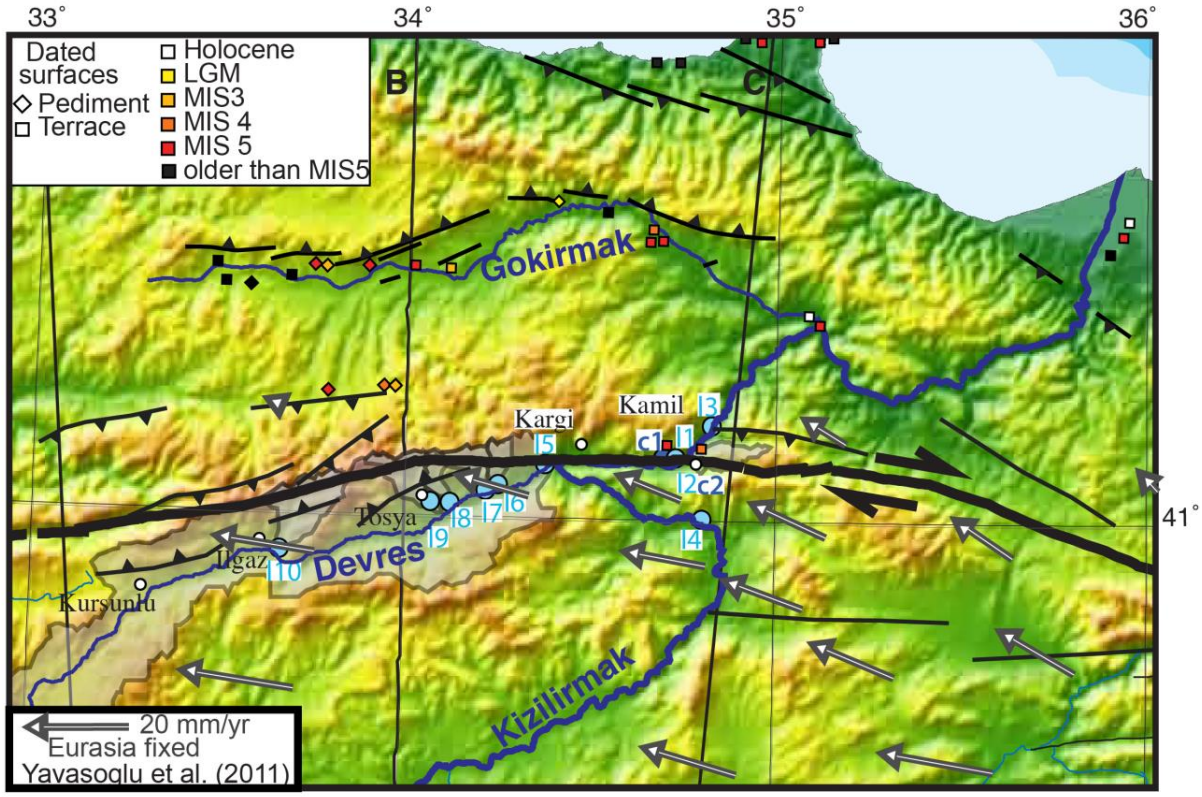


**Figure 8.** The convex NAF central arc forming an orogenic wedge associated with thrust faulting. GPS vectors from *Yavaşoğlu et al.* [2011] outlined the expected convergence in the region of Kargı, Kamil, Tosya and Ilgaz. Dated ulipfted surfaces are indicated with colors for their exposure ages (north of the Kızılırmak, work of *Yıldırım et al.* [2013a and b] and *Berndt et al.* [2018]. Location of sand samples for erosion rates are indicated with blue circles, the catchment of the Devres River is outlined in gray.

Subsequent incision would be related to a modification of the erosional capacity of the river related to change in discharge and sediment load linked to vegetation and climatic changes [*Fuller et al.,* 2009]. This episode is broadly recorded in the whole Mediterranean area. Indeed, according to *Macklin et al.* [2002], the largest alluviation in the Mediterranean area took place around 88 ka. This major river aggradation episode has been related to accelerated catchment erosion and lacustrine sedimentation [*Allen et al.,* 1999; *Fuller et al.,* 1998; *Macklin et al.,* 2002].

The 68±6ka age of **T2** also corresponds to the ages of strath terrace (i.e. 68±6 ka, $^{36}$Cl age) and pediments (60±5 ka $^{10}$Be age; 70±7 ka $^{21}$Ne age) in the Gökırmak catchment [*Yıldırım et al.,* 2013a] (Figure 8). **T2** would thus result from another regional episode of planation level that occurred during MIS4 (60-75 ka). This planation is lightly older than the youngest strath terrace formation in the Filyos Basin at 50.9±2.8 ka [*McClain et al.,* 2017] (Figure 1a), but it corresponds also to a ~60ka alluvial optima documented in the Duzce Basin [*Pucci et al.,* 2008]. This time period corresponds to a large climate degradation recorded in the Sofular Cave located 100 km west of our study area [*Fleitmann et al.,* 2009] and in the Lake Van record in eastern Turkey. There, the pollen record evidences the nearly complete disappearance of arboreal pollen (Pinius and Quercus) [*Litt et al.,* 2014; *Pickarski et al.,* 2015], which was synchronous with the second largest decrease in water level during the last 90 ka [Çağatay et al., 2014] and with the emplacement of lowstand deltas [*Cukur et al.,* 2014]. Changes in vegetation and in catchment hydrology, which are the primary control of sedimentation, may have triggered this second episode of strath planation in the Kamil Basin. In the Mediterranean, there are few alluvium record from the MIS4 period [*Macklin et al.*, 2002], so this strath planation episode could be specific to the Eastern Mediterranean area.

In Kamil, **T1** and **T0** attest for a large fluvial aggradation [*Fraser et al.,* 2010a]. The ~25 m thick T1 aggradational fill corresponds to a large sediment delivery (Figure 2d). About 30 km more to the west, in the Kargi Basin, a fill terrace standing 30 m above the floodplain also exists. In the CAP, a large ~18m thick sediment infill at 15,390±150yrs $^{14}$C BP [i.e 16.5 cal ka ago; *Doğan,* 2011] was also evidenced in the Kızılırmak floodplain. According to *Doğan* [2011], it occurred after a main downcutting phase of the river, which started after later stages of MIS 5 or early MIS 4.This downcutting to aggradation change occurred during the most pronounced climate change in the Mediterranean area, the last glacial–interglacial transition [*Langgut,* 2011]. The LGM to Holocene transition in Turkey is characterized by drastic vegetation [e.g. *Valsecchi et al.,* 2012], precipitation [*Jones et al.,* 2007] and temperature changes [*Göktürk et al.,* 2011]. The LGM has specific characteristics in Anatolia. First, evapotranspiration ratio was low, so there was a positive water balance with high lake levels in Anatolian [*Roberts et al.,* 2011; *Jones et al.,* 2007]. Second, high snowfall and restricted vegetation cover were resulting in strong river discharge. *Doğan* [2010] inferred that these two factors leaded to a high discharge/sediment supply ratio during the glacial period in Turkey resulting in valley downcutting. The change during the Holocene transition to a more negative hydraulic balance resulted in a shift from downcutting to aggradational filling along the Kızılırmak as evidenced in the CAP. *Pucci et al.* [2008] also documented this alluviation phase at the transition from arid to humid conditions in the Duzce Basin. We thus inferred that T1 in the Kamil Basin resulted from the same process and was emplaced during the LGM to Holocene transition.

The terraces in the Kamil Basin are thus a response to climatic fluctuations like at other upstream and downstream locations along the Kızılırmak River [i.e. *Yıldırım et al.,* 2013a; *Doğan,* 2011; *Çiner et al.,* 2005]. Other river terraces in Turkey [*Westaways et al.,* 2004], in the Mediterranean area [*Bridgland,* 2000; *Macklin et al.,* 2002] have also systematically been attributed to climate forcing.

## 6.2 Geological strike-slip motion along the NAF

**T3** provides some constrains on the NAF quaternary slip rate. We documented a 750 m long offset of T3 risers and of the Koz stream. The incision of the Koz River has separated the **eastern** and **western T3** surfaces and predates the emplacement of marble cobble by frost cracking. The 750 m offset would thus be older than 55 ka, the age of the oldest marble cobbles on the **western T3** surface bought by frost-cracking. Similarly, the T3 riser offset is younger than **T3** bevelling at 85±15ka. The geological slip rate on the NAF can thus be bracketed between 8 mm/yr and 14 mm/yr.

The obtained slip rate can be compared to other geological rates. The upper bound of our geological rate is compatible with the lower bound of Holocene slip nearby [*Hubert-Ferrari et al.,* 2000; *Kozacı et al.,* 2007; *Kozacı et al.,* 2009] (see section 2.1). The Kamil rate can also be compared to the longer term geological slip rate obtained considering that the Kızılırmak established its course across the CP ~2 Ma [*Hubert-Ferrari et al.,* 2000; *Yıldırım et al.,* 2011] and its 30 km long offset between the Kamil and the Kargi pull-apart. The resulting geological rate of 15 mm/yr over 2 Ma corresponds well to maximum slip rate inferred in Kamil.

However, the maximum slip rate obtained is lower than the geodetic rate inferred using a local network measured (17 to 22 mm/yr) [*Yavaşoğlu et al.,* 2011] and using Insar velocity profiles (21 mm/yr, average with 14-29 mm/yr 95%CI) [*Hussain et al.,* 2016]. Lower geological rates compared to geodetic rates can be linked to different factors. First, even if most of the deformation takes places on the NAF offsetting **T3**, a small part can be accommodated on a relatively broad zone around. Indeed, the geology is composed of a serie of amalgamated terrains separated by various inactive E-W fault structures that are optimally oriented in the present-day stress field to accommodate some deformation. In that case, *Vallage et al.* [2016] have shown that geologic structures can accommodate a significant part of the deformation in a band associated with the main long-term fault plane. Second, the geodetic and Insar data may also not be fully representative of the geological time-scale deformations. This is the case for the Karakorum strike-slip faut whose geological rate is 10 times larger that its geodetic rates [*Chevalier et al.,* 2005]. Similarly, the Garlock Fault in California shows no present-day accumulating deformation, but it has a ~ 5mm/yr geological slip rate [*Peltzer et al.,* 2011]. Reconciling both rates would require non-steady mantle flow and lower crustal fault creep [*Chuang and Johnson,* 2011]. These two options were already debated by *Gasperini et al.* [2011] in the Marmara

615 region, as they obtained a NAF geological slip rate that is about one half of the one expected from plate-motion
616 [*Polonia et al.,* 2004]. Along the NAF, both mechanisms may be at play.
617

618 ## 6.3 Uplift gradient in the Central Pontides

619
620 T3 and T2 also provide information on the river incision rate and rock uplift over the last 130 ka in the CP. Given
621 the height and age of the terraces, an identical incision rate of 1mm/yr is inferred for both terraces. The obtained
622 incision rate based on two terrace remnants is integrated over a glacial/interglacial cycle and can thus be applied as a
623 proxy for uplift following *Hancock and Anderson* [2002] or *Wegmann and Pazzaglia* [2002]. In the Gökırmak
624 watershed located just north of the Kamil Basin, river incision rates were similarly inferred to represent uplift rates
625 (Figure 8) [*Yıldırım et al.,* 2013a].
626
627 Our rate can be compared to the 0.28 mm/yr rate [*Yıldırım et al.,* 2013a] derived in the Gökırmak catchment located
628 40 km to the northeast because they are not separated by a knickpoint (Figure 8). The fluvial incision rate at Kamil
629 by the Kızılırmak River is 3 times higher that the fluvial incision rate in the Gökırmak catchment. The uplift rate
630 close to the NAF is thus three times higher than in the Sinop Range to the north. This conclusion is in agreement
631 with the CP topography as investigated by *Yıldırım et al.* [2011] and illustrated in the present paper by topographic
632 sections (Figure 1). The CP close to the NAF shows higher fluvial base levels, higher ridge levels and higher relief
633 compare to the Sinop range to the north (Figure 8).
634
635 The larger incision rate at the study location is also in agreement with the proposed tectonic model of the area. The
636 CP are interpreted as a positive flower structure related to the convex bend of the NAF that is too narrow to
637 accommodate without off-fault deformation the rotation of the Anatolian Plate. According to *Yıldırım et al.* [2013a],
638 the related shortening is accommodated in a wide orogenic wedge, which reaches the Black Sea Coast and is
639 responsible for the uplift of the CP. We evidence a non-uniform uplift within the CP Wedge with higher rate close to
640 the NAF. It implies that the transpressional deformation is not accommodated evenly within the wedge. Therefore
641 even regarding shortening in the orogenic wedge, the NAF is still the main structure in the deformation pattern.
642

643 ## 6.4 Erosion Rates, cumulated shortening and the role of the NAF

644 The 395 mm/ka average erosion rate from the CP Rivers ranging is significantly higher than the 40 mm/ka erosion
645 rate of the CAP [*Aydar et al.,* 2013]. We compared them to the present-day sediment discharge (solid phase) of
646 some of the largest rivers in Turkey draining from the CAP to the Black Sea coast. The Sakarya, Kızılırmak and
647 Yesilirmak Rivers are transporting, respectively 8.8 Mt/yr, 23 Mt/yr, and 19 Mt/yr as bedload [*Meybeck et Ragu,*
648 1995]. Given their respective drainage area and an average density of 2.7, an average erosion rate of 120 mm/ka can
649 thus be obtained. The present-day average discharge at the river outlets is thus compatible with the longer-term
650 denudation rates characterizing the CAP and the higher ones across the CP.
651
652 The basin average erosion rates are at least two times lower than the 1mm/yr incision rate of the Kızılırmak River.
653 As a result the Kızılırmak and Devres Rivers form marked V shaped valleys across the CP with a relief reaching
654 over 1500 m (Figure 1).
655
656 We use erosion rates and relief to retrieve a first order mass balance of the CP (Figure 9). We evaluate a first order
657 cumulated shortening in the CP using the relief formed above a fixed reference (i.e the theoretical topography in the
658 region without deformation). Our reference level is the Kızılırmak base-level because of its very low incision rate
659 across the CAP (i.e. 50 mm/ka) [*Çiner et al.,* 2015] and the low erosion rate of the plateau itself (i.e. 40 mm/ka)
660 [Aydar et al., 2013]. Farther north, it is also an adequate reference if we consider a steady state equilibrium of the
661 landscape with an incision rate equal to the uplift rate; its geometry is similar to the strait extension of the
662 Kızılırmak base-level from CAP to the Black Sea coast.

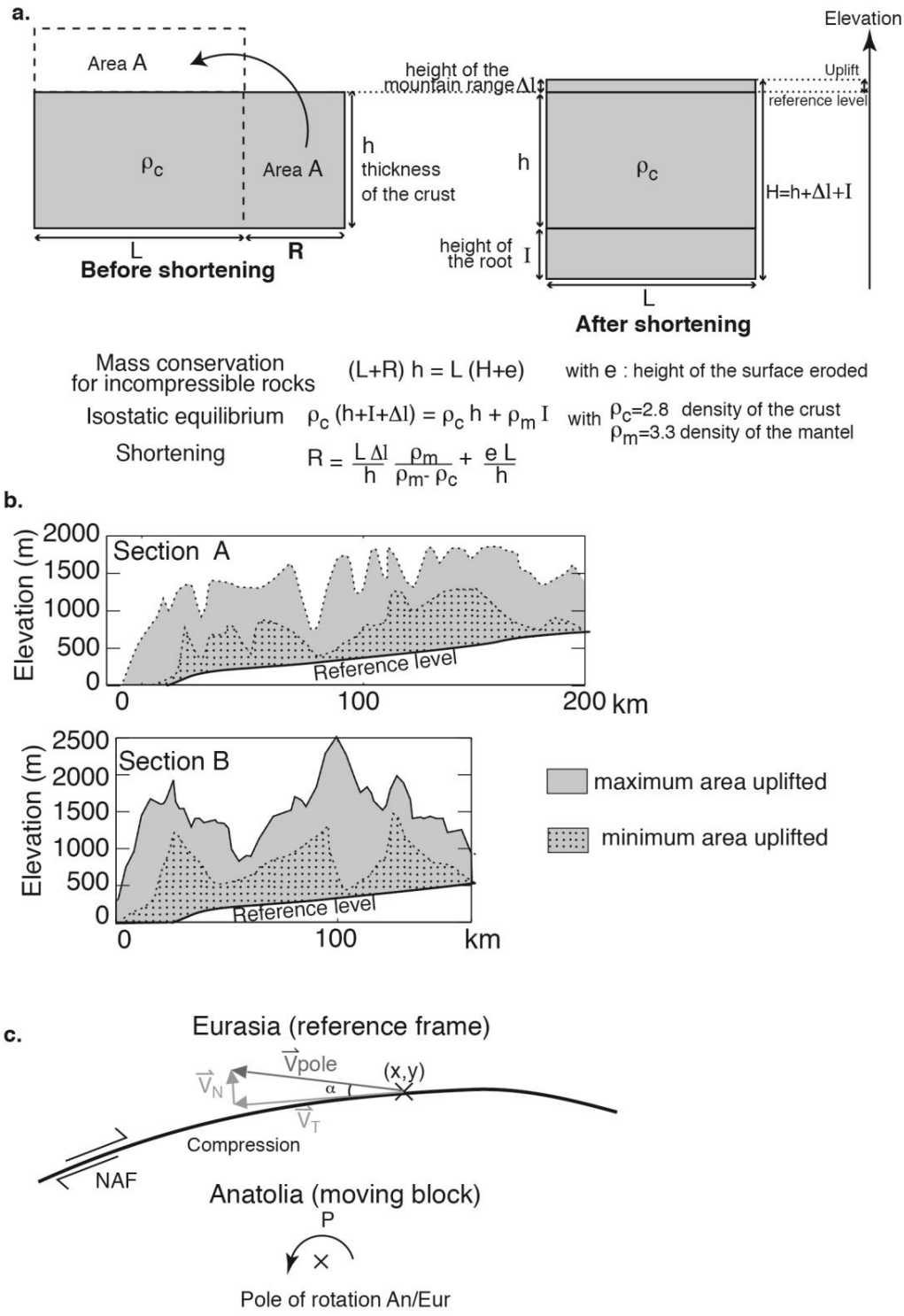


**Figure 9.** First order shortening in the CP. **a**. Mass balance considering isostasy, erosion and a cumulated shortening R. **b**. Minimal and maximal uplifted surfaces along profiles A and B with respect to the reference level (Figure 1). Once the surfaces are computed, shortening can be computed. **c**. Shortening derived from the geometry of the NAF that is different from the small

circle of the rotation pole of Anatolia/Eurasian or from GPS vectors that form an angle with respect to the NAF central bend. A cumulated Anatolian motion of 85 km would imply a 9 km shortening in the NAF central bend, if the Anatolia/Eurasia kinematics and NAF geometry stayed constant.

On profiles A and B in Figure 1 across the CP, the minimal uplifted area lies in between the lowest topographic level and the reference level (Figure 9b). Considering (1) an isostatic equilibrium, (2) a width of the range of about 200 km, (3) a crust of 30 to 40 km [*Makris and Stobbe* 1984; *Vanacore et al.,* 2013], and (4) density of 2.8 and 3.3 for the crust and the mantle, we obtain a minimal shortening of 12 km to 16 km. Considering a minimal erosion rate of about 120 mm/ka, we would need to add a shortening of 1.2 km over the last 2 Ma, and 3 km over the last 5 Ma.

This shortening rate is compared to the long-term shortening induced by the NAF geometry in its central convex bend over its history (Figure 9c). Considering a cumulated lateral motion of the Anatolian Block of about 85 km [e.g. *Hubert-Ferrari et al.,* 2002] along the small circle that best approximates the NAF trace from Erzincan in the East to the Marmara Sea in the west (Figure 1), we obtain a 9 km cumulated shortening in its central part. This inferred shortening is significantly lower than the minimal shortening inferred in the CP. A first reason is that the NAF is not the only driver of the shortening. Part of the stress related to the Arabia-Eurasion collision may be transmitted across Anatolia to the north, and concentrated at the border with the more rigid oceanic lithosphere of the Black Sea. This would explain the large relief formed by the CP continuously along the whole southern Black Sea coast and the higher elevations more to east toward the Lesser Caucasus. A second possibility is that part of the shortening is inherited and might be linked to the westward NAF propagation process. In the central bend area, the NAF encounters a large number of former active faults, as the CP has a rich tectonic history and represents an amalgamation of various terrains since the Jurassic. Because of the large number of E-W trending tectonic pre-existing structures, a distributed deformation prior to the NAF emplacement as a main structure all the way to the surface, is likely to have taken place. This process was already inferred in *Hubert-Ferrari et al.* [2002] and was documented father west in the Marmara Sea [*Karakaş et al.,* 2018].

## 7 Conclusion

Geomorphic mapping, $^{14}C$ dating and measurements of cosmogenic nuclide concentration in riverbeds and in cobbles on strath terraces constrain the deformation pattern of the central transpressive arc of the NAF over different scales. In the Kamil Basin, T0 the most recent fill terrace was offset by ~14±2m during the last two major 1943 and 1668 earthquakes, which implies that the displacement per event along the 1943 segment is variable between seismic cycles, a pattern opposite to the 1944 segment [*Kondo et al.,* 2010]. A larger 750 m offset of T3 was evidenced, which suggests a maximum geological slip rate of 14 mm/yr compatible with the longer-term of 30 km offset of the Kızılırmak River over the last 2 Ma. Geological slip rates are smaller than the geodetic rates, which suggests that distributed deformation took place across the numerous inherited E-W trending structures of the CP. Terrace incision constrain uplift in the CP. T3 and T2 strath terraces have respective exposure ages of 85 ± 15 ka and 66±7 ka. T3 corresponds to a major Mediterranean river aggradation associated this a high denudation rate in the mountains, and T2 to a more local one. T3 and T2 stand 95 and 75 m above the Kızılırmak floodplain, respectively, and their incision provided constraints regarding uplift in the CP. The resulting 1 mm/yr uplift rate is higher than the 0.28 mm/yr one in the Gökırmak catchment just to the north [*Yıldırım et al.,* 2013a]. Transpressive deformation in the central orogenic wedge is thus not accommodated uniformly and is higher at the center of the flower structure formed by the NAF. Finally, we evidenced (1) a 160 m/Ma minimum denudation rate of the Kızılırmak catchment in the CP, which is 3 times higher than in the CAP, and (2) higher cosmogenic nuclide denudation rates in catchments directly affected by thrust faulting; both results suggest a strong tectonic control of erosion rates in the CP and broadly in Anatolia. Erosion rates and relief above the Kızılırmak base level were combined to infer a minimal shortening rate of 15 to 19 km in the CP. It is significantly larger than the local cumulated shortening induced by the NAF restraining geometry in its central part. We thus infer that the origin of the present-day relief in the CP is partly related to compressive stresses linked to the Arabian-Eurasian collision that are transmitted through the CAP and concentrated on amalgamated faulted terrains lying against a more homogeneous Black Sea oceanic crust.

## Acknowledgments

Our field study was greatly enhanced by the organizing assistance of Erhan Altunnel from Osmangazi University, Eskishir, Turkey. The trenches were opened with the help of Jeff Frasers. Many thanks to Sevgi Altinok and Cagil Karakas for help in the field. We acknowledge the European Commission for funding this project as part of the Marie Curie Excellence Grant Project "Understanding the Irregularity of Seismic Cycles: A Case Study in Turkey" (MEXT-CT-2005-025617: Seismic Cycles). Supplemental information and data would be found on the Open Repository and Bibliography of the University of Liege (https://orbi.uliege.be/).

## References

Akçar, N., Yavuz, V., Ivy-Ochs, S., Reber, R., Kubik, P. W., Zahno, C., & Schlüchter, C. (2014). Glacier response to the change in atmospheric circulation in the eastern Mediterranean during the Last Glacial Maximum. Quaternary Geochronology, 19, 27-41.

Allen, J. R., Brandt, U., Brauer, A., Hubberten, H. W., Huntley, B., Keller, J., Kraml, M., Mackensen, A., Mingram, J., Negendank, Nowaczyk, N. R., Oberhansli, H., Watts, W.A., Wulf, S., Zolitschka, B. (1999). Rapid environmental changes in southern Europe during the last glacial period. Nature, 400(6746), 740.

Allmendinger, R. W., R. Reilinger, and J. Loveless (2007), Strain and rotation rate from GPS in Tibet, Anatolia, and the Altiplano, Tectonics, 26, TC3013, doi:10.1029/2006TC002030.

Ambraseys, N. N. (1970). Some characteristic features of the Anatolian fault zone. Tectonophysics, 9(2-3), 143-165.

Anderson RS & Anderson SP (2010). Geomorphology: The Mechanics and Chemistry of Landscapes. xvi+ 637pp. Cambridge University Press. ISBN 978 0 521 51978 6.

Anderson, R. S., Anderson, S. P., & Tucker, G. E. (2013). Rock damage and regolith transport by frost: An example of climate modulation of the geomorphology of the critical zone. Earth Surface Processes and Landforms, 38(3), 299-316.

Andrieux, J., Över, S., Poisson, A., & Bellier, O. (1995). The North Anatolian Fault Zone: distributed Neogene deformation in its northward convex part. Tectonophysics, 243(1-2), 135-154.

Applegate, P. J., Urban, N. M., Keller, K., Lowell, T. V., Laabs, B. J., Kelly, M. A., & Alley, R. B. (2012). Improved moraine age interpretations through explicit matching of geomorphic process models to cosmogenic nuclide measurements from single landforms. Quaternary Research, 77(2), 293-304. Armijo, R., Lyon-Caen, H., & Papanastassiou, D. (1992). East-west extension and Holocene normal-fault scarps in the Hellenic arc. Geology, 20(6), 491-494.

Armitage, J. J., Duller, R. A., Whittaker, A. C., & Allen, P. A. (2011). Transformation of tectonic and climatic signals from source to sedimentary archive. Nature Geoscience, 4(4), 231.

Arnold, Maurice, et al. "The French accelerator mass spectrometry facility ASTER: improved performance and developments." Nuclear Instruments and Methods in Physics Research Section B: Beam Interactions with Materials and Atoms 268.11-12 (2010): 1954-1959.

Aydar, E., Cubukcu, H. E., Şen, E., & Akın, L. (2013). Central Anatolian Plateau, Turkey: incision and paleoaltimetry recorded from volcanic rocks. Turkish J Earth Sci, 22, 739-746.Badertscher, S., Fleitmann, D., Cheng, H., Edwards, R. L., Göktürk, O. M., Zumbühl, A., ... & Tüysüz, O. (2011). Pleistocene water intrusions from the Mediterranean and Caspian seas into the Black Sea. Nature Geoscience, 4(4), 236.

Balco, G., Stone, J. O., Lifton, N. A., & Dunai, T. J. (2008). A complete and easily accessible means of calculating surface exposure ages or erosion rates from 10Be and 26Al measurements. Quaternary geochronology, 3(3), 174-195.

Ballato, P., Parra, M., Schildgen, T. F., Dunkl, I., Yıldırım, C., Özsayın, E., ... & Strecker, M. R. (2018). Multiple exhumation phases in the Central Pontides (N Turkey): New temporal constraints on major geodynamic changes associated with the closure of the Neo-Tethys Ocean. Tectonics, 37(6), 1831-1857.

Barka, A. A., & Hancock, P. L. (1984). Neotectonic deformation patterns in the convex-northwards arc of the North Anatolian fault zone. Geological Society, London, Special Publications, 17(1), 763-774.

Barka, A. A. (1984). Geology and tectonic evolution of some Neogene-Quaternary basins in the North Anatolian fault zone, special publication. Geol. Soc. of Turk, 209-227.

Barka, A. A., & Kadinsky-Cade, K. (1988). Strike-slip fault geometry in Turkey and its influence on earthquake activity. Tectonics, 7(3), 663-684.

Barka, A. (1996). Slip distribution along the North Anatolian fault associated with the large earthquakes of the period 1939 to 1967. Bulletin of the Seismological Society of America, 86(5), 1238-1254.

Benedetti, L., Finkel, R., Papanastassiou, D., King, G., Armijo, R., Ryerson, F., ... & Flerit, F. (2002). Post-glacial slip history of the Sparta fault (Greece) determined by 36Cl cosmogenic dating: Evidence for non-periodic earthquakes. Geophysical Research Letters, 29(8), 87-1.

Berndt, C., Yıldırım, C., Çiner, A., Strecker, M. R., Ertunç, G., Sarıkaya, M. A., ... & Kiyak, N. G. (2018). Quaternary uplift of the northern margin of the Central Anatolian Plateau: New OSL dates of fluvial and delta-terrace deposits of the Kızılırmak River, Black Sea coast, Turkey. Quaternary Science Reviews, 201, 446-469.

Bierman, P., & Steig, E. J. (1996). Estimating rates of denudation using cosmogenic isotope abundances in sediment. Earth surface processes and landforms, 21(2), 125-139.

Borchers, B., Marrero, S., Balco, G., Caffee, M., Goehring, B., Lifton, N., ... & Stone, J. (2016). Geological calibration of spallation production rates in the CRONUS-Earth project. Quaternary Geochronology, 31, 188-198.

Bridgland, D. R. (2000). River terrace systems in north-west Europe: an archive of environmental change, uplift and early human occupation. Quaternary Science Reviews, 19(13), 1293-1303.

Brown, E. T., Bourlès, D. L., Colin, F., Raisbeck, G. M., Yiou, F., & Desgarceaux, S. (1995). Evidence for muon-induced production of 10Be in near-surface rocks from the Congo. Geophysical Research Letters, 22(6), 703-706.

Brown, E. T., Molnar, P., and Bourlés, D. L., 2005. Comment on "Slip-rate measurements on the 630 Karakorum Fault may imply secular variations in fault motion." Science 309, 1326b.

Burbank, D. W., & Anderson, R. S. (2009). Tectonic geomorphology. John Wiley & Sons.

Çağatay, M. N., Öğretmen, N., Damcı, E., Stockhecke, M., Sancar, Ü., Eriş, K. K., & Özeren, S. (2014). Lake level and climate records of the last 90ka from the Northern Basin of Lake Van, eastern Turkey. Quaternary Science Reviews, 104, 97-116.

Cavalié, O., & Jónsson, S. (2014). Block-like plate movements in eastern Anatolia observed by InSAR. *Geophysical Research Letters*, *41*(1), 26-31.

Cavazza, C., I. Federici, A. I. Okay, and M. Zattin (2012), Apatite fissiontrack thermochronology of the Western Pontides (NW Turkey), Geol. Mag., 149, 133–140.

Çiner, A., Doğan, U., Yıldırım, C., Akçar, N., Ivy-Ochs, S., Alfimov, V., ... & Schlüchter, C. (2015). Quaternary uplift rates of the Central Anatolian Plateau, Turkey: insights from cosmogenic isochron-burial nuclide dating of the Kızılırmak River terraces. Quaternary Science Reviews, 107, 81-97.

Çinku, M. C., Hisarlı, Z. M., Heller, F., Orbay, N., & Ustaömer, T. (2011). Middle Eocene paleomagnetic data from the eastern Sakarya Zone and the central Pontides: Implications for the tectonic evolution of north central Anatolia. Tectonics, 30(1).

Chevalier, M. L., Ryerson, F. J., Tapponnier, P., Finkel, R. C., Van Der Woerd, J., Haibing, L., & Qing, L. (2005). Slip-rate measurements on the Karakorum fault may imply secular variations in fault motion. science, 307(5708), 411-414.

Chmeleff, J., von Blanckenburg, F., Kossert, K., Jakob, J. (2010). Determination of the 10Be half-life by multicollector ICP-MS and liquid scintillation counting. Nuclear Instruments and Methods in Physics Research B 268, 192- 199.

Chuang, R. Y., & Johnson, K. M. (2011). Reconciling geologic and geodetic model fault slip-rate discrepancies in Southern California: Consideration of nonsteady mantle flow and lower crustal fault creep. Geology, 39(7), 627-630.

Cukur, D., Krastel, S., Schmincke, H. U., Sumita, M., Çağatay, M. N., Meydan, A. F., ... & Stockhecke, M. (2014). Seismic stratigraphy of lake Van, eastern Turkey. Quaternary Science Reviews, 104, 63-84.

Daout, S., S. Barbot, G. Peltzer, M.-P. Doin, Z. Liu, and R. Jolivet (2016). Constraining the kinematics of metropolitan Los Angeles faultswith a slip-partitioning model, Geophys. Res. Lett., 43, 11,192–11,201 doi:10.1002/2016GL071061.

D'Arcy, M., Roda-Boluda, D. C., & Whittaker, A. C. (2017). Glacial-interglacial climate changes recorded by debris flow fan deposits, Owens Valley, California. Quaternary Science Reviews, 169, 288-311.

Desilets, D., Zreda, M., & Prabu, T. (2006). Extended scaling factors for in situ cosmogenic nuclides: new measurements at low latitude. Earth and Planetary Science Letters, 246(3-4), 265-276.

Doğan, U. (2010). Fluvial response to climate change during and after the Last Glacial Maximum in Central Anatolia, Turkey. Quaternary International, 222(1-2), 221-229.

Doğan, U. (2011). Climate-controlled river terrace formation in the Kızılırmak Valley, Cappadocia section, Turkey: inferred from Ar–Ar dating of Quaternary basalts and terraces stratigraphy. Geomorphology, 126(1-2), 66-81.

Edmond, J. M., & Huh, Y. (1997). Chemical weathering yields from basement and orogenic terrains in hot and cold climates. In Tectonic uplift and climate change (pp. 329-351). Springer, Boston, MA.

Farber, D. L., Mériaux, A. S., & Finkel, R. C. (2008). Attenuation length for fast nucleon production of 10Be derived from near-surface production profiles. Earth and Planetary Science Letters, 274(3-4), 295-300.

Fleitmann, D., Cheng, H., Badertscher, S., Edwards, R. L., Mudelsee, M., Göktürk, O. M., ... & Kramers, J. (2009). Timing and climatic impact of Greenland interstadials recorded in stalagmites from northern Turkey. Geophysical Research Letters, 36(19).

Fraser, J., Vanneste, K., & Hubert-Ferrari, A. (2010). Recent behavior of the North Anatolian Fault: Insights from an integrated paleoseismological data set. Journal of Geophysical Research: Solid Earth, 115(B9).

Fraser, J., Hubert-Ferrari, A., Vanneste, K., Altinok, S., & Drab, L. (2010). A relict paleoseismic record of seven earthquakes between 2000 BC and 600 AD on the central North Anatolian fault at Elmacik, near Osmancik, Turkey. Bulletin, 122(11-12), 1830-1845.

Fuller, I. C., Macklin, M. G., Lewin, J., Passmore, D. G., & Wintle, A. G. (1998). River response to high-frequency climate oscillations in southern Europe over the past 200 ky. Geology, 26(3), 275-278.

Fuller, T. K., Perg, L. A., Willenbring, J. K., & Lepper, K. (2009). Field evidence for climate-driven changes in sediment supply leading to strath terrace formation. Geology, 37(5), 467-470.

Gasperini, L., Polonia, A., Çağatay, M. N., Bortoluzzi, G., & Ferrante, V. (2011). Geological slip rates along the North Anatolian Fault in the Marmara region. Tectonics, 30(6).

Göktürk, O. M., Fleitmann, D., Badertscher, S., Cheng, H., Edwards, R. L., Leuenberger, M., ... & Kramers, J. (2011). Climate on the southern Black Sea coast during the Holocene: implications from the Sofular Cave record. Quaternary Science Reviews, 30(19-20), 2433-2445.

Gosse, J. C., & Phillips, F. M. (2001). Terrestrial in situ cosmogenic nuclides: theory and application. Quaternary Science Reviews, 20(14), 1475-1560.

Granger, D. E., Kirchner, J. W., & Finkel, R. (1996). Spatially averaged long-term erosion rates measured from in situ-produced cosmogenic nuclides in alluvial sediment. The Journal of Geology, 104(3), 249-257.

Granger, D. E., & Smith, A. L. (2000). Dating buried sediments using radioactive decay and muogenic production of 26Al and 10Be. Nuclear Instruments and Methods in Physics Research Section B: Beam Interactions with Materials and Atoms, 172(1-4), 822-826.

Hales, T. C., & Roering, J. J. (2007). Climatic controls on frost cracking and implications for the evolution of bedrock landscapes. Journal of Geophysical Research: Earth Surface, 112(F2).

Hancock, G. S., & Anderson, R. S. (2002). Numerical modeling of fluvial strath-terrace formation in response to oscillating climate. Geological Society of America Bulletin, 114(9), 1131-1142.

Hetzel, R., Niedermann, S., Tao, M., Kubik, P. W., & Strecker, M. R. (2006). Climatic versus tectonic control on river incision at the margin of NE Tibet: 10Be exposure dating of river terraces at the mountain front of the Qilian Shan. Journal of Geophysical Research: Earth Surface, 111(F3).

Herece E. and Akay E., 2003, Atlas of North Anatolian Fault (NAF). General Directorate of Mineral Research and Exploration, Special Publication series-2, Ankara, 61 p+13 appendices as separate maps.

Hubert-Ferrari, A., R. Armijo, B. Meyer, G.C.P. King and A. Barka (2002). Morphology, displacement and slip rates along the North Antolian Fault (Turkey), J. Geophys. Res., 107; doi:10.1029/2001JB000393.

Hussain, E., Hooper, A., Wright, T. J., Walters, R. J., & Bekaert, D. P. (2016). Interseismic strain accumulation across the central North Anatolian Fault from iteratively unwrapped InSAR measurements. Journal of Geophysical Research: Solid Earth, 121(12), 9000-9019.

Hussain, E., Wright, T. J., Walters, R. J., Bekaert, D. P., Lloyd, R., & Hooper, A. (2018). Constant strain accumulation rate between major earthquakes on the North Anatolian Fault. Nature communications, 9(1), 1392.

~~Ivy-Ochs, S., & Schaller, M. (2009). Examining processes and rates of landscape change with cosmogenic radionuclides. Radioactivity in the Environment, 16, 231-294.~~

Jones, M. D., Roberts, C. N., & Leng, M. J. (2007). Quantifying climatic change through the last glacial–interglacial transition based on lake isotope palaeohydrology from central Turkey. Quaternary Research, 67(3), 463-473.

Karakaş, Ç., Armijo, R., Lacassin, R., Suc, J. P., & Melinte-Dobrinescu, M. C. (2018). Crustal strain in the Marmara pull-apart region associated with the propagation process of the North Anatolian Fault. Tectonics, 37(5), 1507-1523.

Karasözen, E., Özacar, A. A., Biryol, C. B., & Beck, S. L. (2013). Seismicity, focal mechanisms and active stress field around the central segment of the North Anatolian Fault in Turkey. Geophysical Journal International, 196(1), 405-421.

Kohl, C. P., & Nishiizumi, K. (1992). Chemical isolation of quartz for measurement of in-situ-produced cosmogenic nuclides. Geochimica et Cosmochimica Acta, 56(9), 3583-3587.

915 Kondo, H., Özaksoy, V., & Yıldirim, C. (2010). Slip history of the 1944 Bolu-Gerede
916 earthquake rupture along the North Anatolian fault system: Implications for recurrence
917 behavior of multisegment earthquakes. Journal of Geophysical Research: Solid Earth,
918 115(B4).

919 Korschinek, G., Bergmaier, A., Faestermann, T., Gerstmann, U.C., Knie, K., Rugel, G.,Wallner,
920 A., Dillmann, I., Dollinger, G., von Gostomski, Lierse Ch., Kossert, K., Maitia,M.,
921 Poutivtsev, M., Remmert, A., 2010. A new value for the half-life of 10Be by Heavy-Ion
922 Elastic Recoil Detection and liquid scintillation counting. Nuclear Instruments and
923 Methods in Physics Research B. 268, 187–191.

924 Kozacı, O., J.F. Dolan, R.C. Finkel and R.D. Hartleb (2007). Late Holocene slip rate for the
925 North Anatolian Fault, Turkey, from cosmogenic 36Cl geochronology: implications for
926 the constancy of fault loading and strain release rates, Geology, 35, 867-870;
927 doi:10.1130/ G23187A.1.

928 Kozacı, Ö., Dolan, J. F., & Finkel, R. C. (2009). A late Holocene slip rate for the central North
929 Anatolian fault, at Tahtaköprü, Turkey, from cosmogenic 10Be geochronology:
930 Implications for fault loading and strain release rates. Journal of Geophysical Research:
931 Solid Earth, 114(B1).

932 Kozacı, O., J. Dolan, O. Yonlü and R. Hartleb (2011). Paleoseismologic evidence for the
933 relatively regular recurrence of infrequent, large-magnitude earthquakes on the eastern
934 North Anatolian Fault at Yaylabeli, Turkey, Lithosphere, 3, 37-54; doi:10.1130/L118.1.

935 Kreemer, C., Holt, W. E., & Haines, A. J. (2003). An integrated global model of present-day
936 plate motions and plate boundary deformation. Geophysical Journal International, 154(1),
937 8-34.

938 Langgut, D., Almogi-Labin, A., Bar-Matthews, M., & Weinstein-Evron, M. (2011). Vegetation
939 and climate changes in the South Eastern Mediterranean during the Last Glacial-
940 Interglacial cycle (86 ka): new marine pollen record. Quaternary Science Reviews,
941 30(27-28), 3960-3972.

942 Le Dortz, K., Meyer, B., Sébrier, M., Nazari, H., Braucher, R., Fattahi, M., ... & Talebian, M.
943 (2009). Holocene right-slip rate determined by cosmogenic and OSL dating on the Anar
944 fault, Central Iran. Geophysical Journal International, 179(2), 700-710.

945 Lifton, N., Sato, T., & Dunai, T. J. (2014). Scaling in situ cosmogenic nuclide production rates
946 using analytical approximations to atmospheric cosmic-ray fluxes. Earth and Planetary
947 Science Letters, 386, 149-160.

948 Litt, T., Pickarski, N., Heumann, G., Stockhecke, M., & Tzedakis, P. C. (2014). A 600,000 year
949 long continental pollen record from Lake Van, eastern Anatolia (Turkey). Quaternary
950 Science Reviews, 104, 30-41.

951 Macklin, M. G., Fuller, I. C., Lewin, J., Maas, G. S., Passmore, D. G., Rose, J., ... & Rowan, J. S.
952 (2002). Correlation of fluvial sequences in the Mediterranean basin over the last 200 ka
953 and their relationship to climate change. Quaternary Science Reviews, 21(14-15), 1633-
954 1641.

Makris, J., & Stobbe, C. (1984). Physical properties and state of the crust and upper mantle of the Eastern Mediterranean Sea deduced from geophysical data. Marine Geology, 55(3-4), 347-363.

Martin, L. C. P., Blard, P. H., Balco, G., Lavé, J., Delunel, R., Lifton, N., & Laurent, V. (2017). The CREp program and the ICE-D production rate calibration database: a fully parameterizable and updated online tool to compute cosmic-ray exposure ages. Quaternary geochronology, 38, 25-49.

Matsuoka, N. (2008). Frost weathering and rockwall erosion in the southeastern Swiss Alps: Long-term (1994–2006) observations. Geomorphology, 99(1-4), 353-368.

McKenzie, D. (1972). Active tectonics of the Mediterranean region. Geophysical Journal of the Royal Astronomical Society, 30(2), 109-185.

McClain, K., Yıldırım, C., Çiner, A., Akif Sarikaya, M., Sahin, S., Özcan, O., ... & Öztürk, T. (2017, April). Quantification of fluvial response to tectonic deformation in the Central Pontides, Turkey; inferences from OSL dating of fluvial terraces. In EGU General Assembly Conference Abstracts (Vol. 19, p. 772).

Mériaux, A. S., Tapponnier, P., Ryerson, F. J., Xiwei, X., King, G., Van der Woerd, J., ... & Wenbin, C. (2005). The Aksay segment of the northern Altyn Tagh fault: Tectonic geomorphology, landscape evolution, and Holocene slip rate. Journal of Geophysical Research: Solid Earth, 110(B4).

Meybeck, M., & Ragu, A. (1995). River discharges to the oceans: An assessment of suspended solids, major ions and nutrients, 245 pp. UN Environ. Programme, Nairobi.Morewood, N. C., & Roberts, G. P. (2000). The geometry, kinematics and rates of deformation within an en échelon normal fault segment boundary, central Italy. Journal of Structural Geology, 22(8), 1027-1047.

Mudd, S. M., Harel, M. A., Hurst, M. D., Grieve, S. W., & Marrero, S. M. (2016). The CAIRN method: automated, reproducible calculation of catchment-averaged denudation rates from cosmogenic nuclide concentrations. Earth Surface Dynamics, 4(3), 655-674.

Mudie, P.J., Marret, F., Aksu, A.E., Hiscott, R.N., Gillespie, H., 2007. Palynological evidence for climatic change, anthropogenic activity and outflow of Black Sea water during the last Pleistocene and Holocene: centennial- to decadal-scale records from the Black and Marmara Seas. Quaternary International 167–168, 73–90.

Nishiizumi, K. (2004). Preparation of 26Al AMS standards. Nuclear Instruments and Methods in Physics Research Section B: Beam Interactions with Materials and Atoms, 223, 388-392.

Okay, A. I., and O. Tüysüz (1999), Tethyan sutures of northern Turkey, in The Mediterranean Basins: Tertiary Extension Within the Alpine Orogen, vol. 156, edited by B. Durand et al., pp. 475–515, Geological Society, London, Special Publication, Oxford, UK.

Ottria, G., Pandolfi, L., Catanzariti, R., Da Prato, S., Ellero, A., Frassi, C., ... & Sayit, K. (2017). Evolution of an early Eocene pull-apart basin in the Central Pontides (Northern Turkey): New insights into the origin of the North Anatolian Shear Zone. Terra Nova, 29(6), 392-400.

995 Over, S., Bellier, O., Poisson, A., Andrieux, J., & Tutkun, Z. (1993). Late Cenozoic fault
996 kinematics within basins along the central North Anatolian fault zone (turkey). Comptes
997 Rendus de l'Académie des Sciens Serie II, 317(6), 827-833.

998 Peltzer, G., Crampé, F., Hensley, S., & Rosen, P. (2001). Transient strain accumulation and fault
999 interaction in the Eastern California shear zone. Geology, 29(11), 975-978.

1000 Piccardi, L., Gaudemer, Y., Tapponnier, P., & Boccaletti, M. (1999). Active oblique extension in
1001 the central Apennines (Italy): evidence from the Fucino region. Geophysical Journal
1002 International, 139(2), 499-530.

1003 Pickarski, N., Kwiecien, O., Djamali, M., & Litt, T. (2015). Vegetation and environmental
1004 changes during the last interglacial in eastern Anatolia (Turkey): a new high-resolution
1005 pollen record from Lake Van. Palaeogeography, Palaeoclimatology, Palaeoecology, 435,
1006 145-158.

1007 Polonia, A., Gasperini, L., Amorosi, A., Bonatti, E., Bortoluzzi, G., Cagatay, N., ... & Seeber, L.
1008 (2004). Holocene slip rate of the North Anatolian Fault beneath the Sea of Marmara.
1009 Earth and Planetary Science Letters, 227(3-4), 411-426.

1010 Portenga, E. W., & Bierman, P. R. (2011). Understanding Earth's eroding surface with 10 Be.
1011 GsA today, 21(8), 4-10.

1012 Pucci, S., De Martini, P. M., & Pantosti, D. (2008). Preliminary slip rate estimates for the Düzce
1013 segment of the North Anatolian Fault Zone from offset geomorphic markers.
1014 Geomorphology, 97(3-4), 538-554.

1015 Reber, R., Akçar, N., Yesilyurt, S., Yavuz, V., Tikhomirov, D., Kubik, P. W., & Schlüchter, C.
1016 (2014). Glacier advances in northeastern Turkey before and during the global Last
1017 Glacial Maximum. Quaternary Science Reviews, 101, 177-192.

1018 Reilinger, R., McClusky, S., Vernant, P., Lawrence, S., Ergintav, S., Cakmak, R., ... & Nadariya,
1019 M. (2006). GPS constraints on continental deformation in the Africa‐Arabia‐Eurasia
1020 continental collision zone and implications for the dynamics of plate interactions. Journal
1021 of Geophysical Research: Solid Earth, 111(B5).

1022 Roberts, N., Reed, J. M., Leng, M. J., Kuzucuoğlu, C., Fontugne, M., Bertaux, J., ... &
1023 Karabiyikoğlu, M. (2001). The tempo of Holocene climatic change in the eastern
1024 Mediterranean region: new high-resolution crater-lake sediment data from central
1025 Turkey. The Holocene, 11(6), 721-736.

1026 Schimmelpfennig, I., Benedetti, L., Finkel, R., Pik, R., Blard, P. H., Bourles, D., ... & Williams,
1027 A. (2009). Sources of in-situ 36Cl in basaltic rocks. Implications for calibration of
1028 production rates. Quaternary Geochronology, 4(6), 441-461.

1029 Schimmelpfennig, I., Benedetti, L., Garreta, V., Pik, R., Blard, P. H., Burnard, P., ... & Dunai, T.
1030 (2011). Calibration of cosmogenic 36 Cl production rates from Ca and K spallation in
1031 lava flows from Mt. Etna (38 N, Italy) and Payun Matru (36 S, Argentina). Geochimica et
1032 Cosmochimica Acta, 75(10), 2611-2632.

1033 Shumilovskikh, L. S., Tarasov, P., Arz, H. W., Fleitmann, D., Marret, F., Nowaczyk, N., Plessen,
1034 B., Schlütz, F., and Behling, H. (2012). Vegetation and environmental dynamics in the

1035 southern Black Sea region since 18 kyr BP derived from the marine core 22-GC3,
1036 Palaeogeogr. Palaeocl., 337–338, 177–193,.

1037 Shumilvskikh, L. S., Arz, H., Fleitmann, D., Marret, F., Nowaczyk, N., Tarasov, P., Wegwerth,
1038 A., and Behling, H. (2013). Vegetation and environmental changes in Northern Anatolia
1039 during penultimate deglaciation and Eemian recorded in Black Sea sediments,
1040 Quaternary Res., 80, 349–360.

1041 Schumilovskikh, L. S., Fleitmann, D., Nowaczyk, N. R., Behling, H., Marret, F., Wegwerth, A.,
1042 & Arz, H. W. (2014). Orbital and millenial-scale environmental changes between 64 and
1043 25 ka BP recorded in Black Sea sediments. Climate of the Past, 10, 939-945.

1044 Şengör, A. M. C., & Yilmaz, Y. (1981). Tethyan evolution of Turkey: a plate tectonic approach.
1045 Tectonophysics, 75(3-4), 181-241.

1046 Şengör, A. M. C., Tüysüz, O., Imren, C., Sakınç, M., Eyidoğan, H., Görür, N., ... & Rangin, C.
1047 (2005). The North Anatolian fault: A new look. Annu. Rev. Earth Planet. Sci., 33, 37-
1048 112.

1049 Siame, L. L., Angelier, J., Chen, R. F., Godard, V., Derrieux, F., Bourlès, D. L., ... & Lee, J. C.
1050 (2011). Erosion rates in an active orogen (NE-Taiwan): A confrontation of cosmogenic
1051 measurements with river suspended loads. Quaternary Geochronology, 6(2), 246-260.

1052 Stone, J.O., 2000. Air pressure and cosmogenic isotope production. Journal of Geophysical
1053 Research 105, 23753–23759.

1054 Tucker, G. E., McCoy, S. W., Whittaker, A. C., Roberts, G. P., Lancaster, S. T., & Phillips, R.
1055 (2011). Geomorphic significance of postglacial bedrock scarps on normal‐fault footwalls.
1056 Journal of Geophysical Research: Earth Surface, 116(F1).

1057 Tapponnier, P., Ryerson, F. J., Van der Woerd, J., Mériaux, A. S., & Lasserre, C. (2001). Long-
1058 term slip rates and characteristic slip: keys to active fault behaviour and earthquake
1059 hazard. Comptes Rendus de l'Académie des Sciences-Series IIA-Earth and Planetary
1060 Science, 333(9), 483-494.

1061 Vallage, A., Klinger, Y., Lacassin, R., Delorme, A., & Pierrot‐Deseilligny, M. (2016).
1062 Geological structures control on earthquake ruptures: The Mw7. 7, 2013, Balochistan
1063 earthquake, Pakistan. Geophysical Research Letters, 43(19), 10-155.

1064 Valsecchi, V., Goni, M. F., & Londeix, L. (2012). Vegetation dynamics in the Northeastern
1065 Mediterranean region during the past 23 000 yr: insights from a new pollen record from
1066 the Sea of Marmara. Climate of the Past, 8(6).

1067 Vanacore, E. A., Taymaz, T., & Saygin, E. (2013). Moho structure of the Anatolian Plate from
1068 receiver function analysis. Geophysical Journal International, 193(1), 329-337.

1069 Van Der Woerd, J., Klinger, Y., Sieh, K., Tapponnier, P., Ryerson, F. J., & Mériaux, A. S.
1070 (2006). Long‐term slip rate of the southern San Andreas fault from 10Be‐26Al surface
1071 exposure dating of an offset alluvial fan. Journal of Geophysical Research: Solid Earth,
1072 111(B4).

Von Blanckenburg, F. (2006). The control mechanisms of erosion and weathering at basin scale from cosmogenic nuclides in river sediment. Earth and Planetary Science Letters, 242(3-4), 224-239.

Wegmann, K. W., & Pazzaglia, F. J. (2002). Holocene strath terraces, climate change, and active tectonics: The Clearwater River basin, Olympic Peninsula, Washington State. Geological Society of America Bulletin, 114(6), 731-744.

Westaway, R., Pringle, M., Yurtmen, S., Demir, T., Bridgland, D., Rowbotham, G., & Maddy, D. (2004). Pliocene and Quaternary regional uplift in western Turkey: the Gediz River terrace staircase and the volcanism at Kula. *Tectonophysics*, *391*(1-4), 121-169.

Wright, T., B. Parsons, and E. Fielding (2001),Measurement of interseismic strain accumulation across the North Anatolian Fault by satellite radar interferometry, Geophys. Res. Lett., 28(10), 2117–2120.

Yavaşoğlu, H., Tarı, E., Tüysüz, O., Çakır, Z., & Ergintav, S. (2011). Determining and modeling tectonic movements along the central part of the North Anatolian Fault (Turkey) using geodetic measurements. Journal of Geodynamics, 51(5), 339-343.

Yıldırım, C., T. F. Schildgen, H. Echtler, D. Melnick, and M. R. Strecker (2011), Late Neogene and active orogenic uplift in the Central Pontides associated with the North Anatolian Fault: Implications for the northern margin of the Central Anatolian Plateau, Turkey, Tectonics, 30, TC5005, doi:10.1029/2010TC002756.

Yıldırım, C., Schildgen, T. F., Echtler, H., Melnick, D., Bookhagen, B., Çiner, A., ... & Strecker, M. R. (2013a). Tectonic implications of fluvial incision and pediment deformation at the northern margin of the Central Anatolian Plateau based on multiple cosmogenic nuclides. Tectonics, 32(5), 1107-1120.

Yıldırım, C., Melnick, D., Ballato, P., Schildgen, T. F., Echtler, H., Erginal, A. E., ... & Strecker, M. R. (2013b). Differential uplift along the northern margin of the Central Anatolian Plateau: inferences from marine terraces. Quaternary Science Reviews, 81, 12-28.

All sources cited in text, tables, figures, and Supporting Information must appear in the main reference list, and all entries in the reference list must be cited in main text. References that are cited in supporting information should also be included in the reference list of the paper and worked into the text, so that they will be indexed and included in citation records and given credit. References are not included in word counts for excess length fees. Data sets that are not newly reported as part of this research should also be cited in the references as a reference. New data sets or software that are deposited elsewhere with a permanent identifier should be cited. AGU follows the Joint Declaration of Data Citations Principles.

All references must be available to readers at the time of publication; there should be no "unpublished" or "in press" references.

An examples of reference:

Deng, A., and D. R. Stauffer (2006), On improving 4-km mesoscale model simulations, J. Appl. Meteorol. Climatol., 45(3), 361–381, doi:10.1175/JAM2341.1.

**Table 1.** $^{10}$Be-$^{26}$Al samples: AMS results, Cronus model age (no inheritance, no erosion), and erosion rates (density 2.7 for all samples). Sample locations in Table S1.

| Samples | Be measurements | | | | Age | Erosion | Al measurements | | | | Age | Erosion |
|---|---|---|---|---|---|---|---|---|---|---|---|---|
| | Quartz (g) | $^{9}$Be carrier (mg) | $^{10}$Be/$^{9}$Be (x10$^{-13}$) | $^{10}$Be (at/g qtz) | $^{10}$Be age (yrs) | $^{10}$Be Erosion rate (m/Ma) | $^{27}$Al natural (mg) | $^{27}$Al carrier added (mg) | $^{26}$Al/$^{27}$Al (x10$^{-13}$) | $^{26}$Al (at/g qtz) | $^{26}$Al age (yrs) | $^{26}$Al Erosion rate (m/Ma) |
| T3-3 | 24 | 0 | 4,56414 ±0,12978 | 613515 ±21328 | 98976 ±9493 | - | 0,86 | 1,30 | 15,09648 ±0,43872 | 3024445 ±185074 | 82243 ±9101 | - |
| T3-4 | 1 | 0 | 0,2505 ±0,01305 | 413535 ±23083 | 63712 ±6684 | - | 0,23 | 2,14 | 0,54527 ±0,05223 | 2840362 ±312111 | 74138 ±10772 | - |
| T3-5 | 21 | 1 | 2,93369 ±0,08785 | 459017 ±16528 | 71273 ±6822 | - | 1,75 | 0,27 | 13,09778 ±0,40262 | 2745533 ±170244 | 72009 ±7963 | - |
| T2-2 | 7,55093 | 0,24825 | 0,93717 ±0,03001 | 206164 ±7782 | 31379 ±2995 | - | 0,55 | 1,33 | 2,31193 ±0,11674 | 1279913 ±94484 | 32606 ±3777 | - |
| T2-5 | 8,87072 | 0,24989 | 0,69218 ±0,03914 | 130471 ±7825 | 20435 ±2168 | - | 4,63 | 0,00 | 0,66174 ±0,06061 | 770359 ±80384 | 20123 ±2759 | - |
| T2-10 | 13,5749 | 0,25188 | 3,50987 ±0,10864 | 435756 ±16059 | 69852 ±6707 | - | 47,04 | 0,00 | not reliable | | | - |
| T2-11 | 20,74936 | 0,50205 | 3,17795 ±0,10378 | 514499 ±19701 | 84799 ±8223 | - | 0,47 | 1,74 | 14,18664 ±0,40934 | 3372687 ±206052 | 94586 ±10526 | - |
| T2-12 | 20,93114 | 0,50572 | 1,2883 ±0,03977 | 208273 ±7660 | 33925 ±3227 | - | 0,81 | 0,65 | 8,55187 ±0,25132 | 1329743 ±81577 | 36281 ±3928 | - |
| T2-13 | 20,54854 | 0,50544 | 2,21847 ±0,06394 | 365127 ±12808 | 57637 ±5478 | - | 0,38 | 1,44 | 8,45114 ±0,26303 | 1665464 ±103589 | 43954 ±4799 | - |
| L1 | 25,7809 | 0,25042 | 0,23857 ±0,03463 | 15505 ±2272 | - | 482 ±120 | 45,41 | 0,00 | 0,00883 ±0,00883 | 34697 ±34742 | - | unreliable |
| L2 | 1,04737 | 0,24772 | 0,0333 ±0,00563 | 52693 ±8970 | - | 134 ±36 | 0,42 | 1,36 | 0,02287 ±0,01144 | 86702 ±43605 | - | 604 ±425 |
| L5 | 25,0548 | 0,25228 | 0,54992 ±0,07113 | 37050 ±4849 | - | 201 ±48 | 53,39 | 0,00 | 0,01458 ±0,01031 | 69295 ±49123 | - | unreliable |
| L6 | 12,22249 | 0,25185 | 0,08488 ±0,01157 | 11702 ±1612 | - | 710 ±170 | 6,41 | 0,00 | 0,01791 ±0,01034 | 20939 ±12135 | - | unreliable |
| L7 | 23,2152 | - | - | - | - | | 56,93 | 0,00 | 0,00949 ±0,00949 | 51902 ±51968 | - | unreliable |
| L8 | 17,3141 | 0,25162 | 0,2671 ±0,01763 | 25972 ±1791 | - | 324 ±67 | 31,51 | 0,00 | 0,04263 ±0,01907 | 173033 ±77873 | - | 360 ±215 |
| L9 | 20,1526 | 0,25043 | - | - | - | | 68,37 | 0,00 | 0,02319 ±0,0116 | 175476 ±88183 | - | 357 ±250 |
| L10 | 21,76207 | 0,50149 | 0,10887 ±0,03148 | 16786 ±4864 | - | 514 ±191 | 46,46 | 0,00 | 0,01785 ±0,0103 | 84977 ±49248 | - | 751 ±672 |
| L3 | 31,4521 | - | - | - | - | - | 63,33 | 0,00 | 0,03234 ±0,01451 | 145228 ±65587 | - | 380 ±220 |
| T3-sand1 | 20,8317 | 0,25132 | 0,9582 ±0,03061 | 77350 ±2915 | | | 19,02 | 0,00 | 0,17923 ±0,0317 | 365033 ±67103 | - | |
| T3-sand2 | 35,03711 | 0,50266 | - | - | | | 50,13 | 0,00 | 0,16636 ±0,03329 | 530841 ±109491 | - | |
| T3-sand3 | 39,4853 | 0,49031 | - | - | | | 43,95 | 0,00 | 0,10279 ±0,03019 | 255196 ±76036 | - | |
| T2-sand1 | 14,0597 | 0,25104 | 0,4378 ±0,09923 | 52304 ±11901 | | | | | | | - | |

**Table 2.** $^{36}$Cl samples : AMS results, model age (no inheritance, no erosion, density 2.7 for all samples). Sample locations in Table S1.

| Sample | $^{36}$Cl (measured) ($10^3$ atoms. $g^{-1}$ rock) | Ages | |
|---|---|---|---|
| | | age | error |
| | | yrs | yrs |
| T3-1 | 3081±61 | 102221 | 11842 |
| T3-2 | 3402±68 | 112409 | 12891 |
| T3-4 | 2225±44 | 71547 | 8143 |
| T3-6 | 2269±45 | 78278 | 8660 |
| T3W-g1 | 925±18 | 28138 | 2934 |
| T3W-g2 | 358±7 | 11115 | 1129 |
| T3W-1 | 858±19 | 25581 | 2674 |
| T3W-2 | 841±19 | 28007 | 2909 |
| T3W-3 | 756±17 | 23082 | 2463 |
| T3W-4 | 680±15 | 21061 | 2230 |
| T3W-5 | 728±16 | 23191 | 2458 |
| T3W-6 | 1063±24 | 34261 | 3677 |
| T3W-7 | 720±16 | 22725 | 2404 |
| T3W-8 | 1627±36 | 50891 | 5615 |
| T3W-9 | 1423±32 | 42424 | 4615 |
| T3W-10 | 1811±40 | 56331 | 6120 |
| T3W-11 | 1298±29 | 39718 | 4329 |
| T3W-12 | 1511±34 | 49078 | 5484 |
| T2-1 | 1503±30 | 50926 | 5560 |
| T2-2 | 1403±28 | 43019 | 4538 |
| T2-3 | 1207±24 | 36705 | 3898 |
| T2-4 | 3176±63 | 107048 | 12108 |
| T2-6 | 881±17 | 26914 | 2771 |
| T2-7 | 1170±23 | 38299 | 4050 |
| T2-8 | 2020±40 | 66816 | 7305 |
| T2-9 | 916±18 | 31428 | 3336 |
| T2-10 | 2312±46 | 73992 | 8509 |
| T2-11 | 2389±47 | 79310 | 9861 |
| T2-12 | 1394±29 | 44567 | 4591 |
| T2-14 | 1449±29 | 48994 | 5334 |